

A Survey on Deep Learning Architectures for Image-based Depth Reconstruction

Hamid Laga

Abstract—Estimating depth from RGB images is a long-standing ill-posed problem, which has been explored for decades by the computer vision, graphics, and machine learning communities. In this article, we provide a comprehensive survey of the recent developments in this field. We will focus on the works which use deep learning techniques to estimate depth from one or multiple images. Deep learning, coupled with the availability of large training datasets, have revolutionized the way the depth reconstruction problem is being approached by the research community. In this article, we survey more than 100 key contributions that appeared in the past five years, summarize the most commonly used pipelines, and discuss their benefits and limitations. In retrospect of what has been achieved so far, we also conjecture what the future may hold for learning-based depth reconstruction research.

Index Terms—Stereo matching, Disparity, CNN, Convolutional Neural Networks, 3D Video, 3D Reconstruction



1 INTRODUCTION

The goal of image-based 3D reconstruction is to infer the 3D geometry and structure of real objects and scenes from one or multiple RGB images. This long standing ill-posed problem is fundamental to many applications such as robot navigation, object recognition and scene understanding, 3D modeling and animation, industrial control, and medical diagnosis.

Recovering the lost dimension from 2D images has been the goal of multiview stereo and Structure-from-X methods, which have been extensively investigated for many decades. The first generation of methods has focused on understanding and formalizing the 3D to 2D projection process, with the aim to devise solutions to the ill-posed inverse problem. Effective solutions typically require multiple images, captured using accurately calibrated cameras. Although these techniques can achieve remarkable results, they are still limited in many aspects. For instance, they are not suitable when dealing with occlusions, featureless regions, or highly textured regions with repetitive features.

Interestingly, we, as humans, are good at solving such ill-posed inverse problems by leveraging prior knowledge. For example, we can easily infer the approximate size and rough geometry of objects using only one eye. We can even guess what it would look like from another view. We can do this because all the previously seen objects and scenes have enabled us to build a prior knowledge and develop mental models of what objects, and the 3D world in general, look like. The second generation of depth reconstruction

methods try to leverage this prior knowledge by formulating the problem as a recognition task. The avenue of deep learning techniques, and more importantly, the increasing availability of large training data sets, have lead to a new generation of methods that are able to recover the lost dimension even from a single image. Despite being recent, these methods have demonstrated exciting and promising results on various tasks related to computer vision and graphics.

In this article, we provide a comprehensive and structured review of the recent advances in image-based depth reconstruction using deep learning techniques. We have gathered more than 100 papers, which appeared from 2014 to December 2018 in leading computer vision, computer graphics, and machine learning conferences and journals dealing specifically with this problem¹. The goal is to help the reader navigate in this emerging field, which gained a significant momentum in the past few years. Compared to the existing literature, the main contributions of this article are as follows;

- To the best of our knowledge, this is the first survey paper in the literature which focuses on image-based depth reconstruction using deep learning techniques.
- We adequately cover the contemporary literature with respect to this area. We present a comprehensive review of more than 100 articles, which appeared from 2014 to December 2018.
- This article also provides a comprehensive review and an insightful analysis on all aspects of depth reconstruction using deep learning, including the training data, the choice of network architectures and their effect on the reconstruction results, the

• Hamid Laga is with Murdoch University (Australia), and with the Phenomics and Bioinformatics Research Centre, University of South Australia. E-mail: H.Laga@murdoch.edu.au

Manuscript received April 19, 2005; revised December 27, 2012.

1. This number is continuously increasing even at the time we are writing this article and during the review process.

training strategies, and the application scenarios.

- We provide a comparative summary of the properties and performances of the reviewed methods for different scenarios including depth reconstruction from stereo pairs, depth reconstruction from multiple images, and depth reconstruction from a single RGB image.

The rest of this article is organized as follows; Section 2 fomulates the problem and lays down the taxonomy. Section 3 focuses on the recent papers that use deep learning architectures for stereo matching. Section 4 reviews the methods that directly regress depth maps from one or multiple images without explicitly matching features across the input images. Section 5 focuses on the training procedures including the choice of training datasets and loss functions. Section 6 discuss the performance of some key methods. Finally, Sections 7 and 8 discuss potential future research directions, and summarize the paper.

2 SCOPE AND TAXONOMY

Let $\mathbf{I} = \{I_k, k = 1, \dots, n\}$ be a set of $n \geq 1$ RGB images of the same 3D scene, captured using cameras whose intrinsic and extrinsic parameters can be *known* or *unknown*. The images can be captured by multiple cameras placed around the 3D scene, and thus they are spatially correlated, or with a single camera moving around the scene producing images that are temporally correlated. The goal is to estimate one or multiple depth maps, which can be from the same viewpoint as the input [1], [2], [3], [4], or from a new arbitrary viewpoint [5], [6], [7], [8], [9]. In this article focuses on methods that estimate depth from one or multiple images with known or unknown camera parameters. Structure-from-Motion (SfM) and Simultaneous Localization and Mapping (SLAM) techniques, which estimate at the same time depth and (relative) camera pose from multiple images or a video stream, are beyond the scope of this article and require a separate survey.

Learning-based depth reconstruction can be summarized as the process of learning a predictor f_θ that can infer a depth map \hat{D} that is as close as possible to the unknown depth map D . In other words, we seek to find a function f_θ such that $\mathcal{L}(\mathbf{I}) = d(f_\theta(\mathbf{I}), D)$ is minimized. Here, θ is a set of parameters, and $d(\cdot, \cdot)$ is a certain measure of distance between the real depth map D and the reconstructed depth map $f_\theta(\mathbf{I})$. The reconstruction objective \mathcal{L} is also known as the *loss function* in the deep learning jargon.

We can distinguish two main categories of methods. Methods in the first class (Section 3) mimic the traditional stereo-matching techniques by explicitly learning how to match, or put in correspondence, pixels across the input images. Such correspondences can then be converted into an optical flow or a disparity map, which in turn can be converted into depth at

each pixel in the input image. The predictor f is composed of three modules: a feature extraction module, a feature matching and cost aggregation module, and a disparity/depth estimation module.

The second class of methods (Section 4) do not explicitly learn the matching function. Instead, they learn a function that directly predicts depth (or disparity) at each pixel in the input image(s). These methods are very general and have been used to estimate depth from a single image as well as from multiple images taken from arbitrary view points. The predicted depth map D can be from the same viewpoint as the input, or from a new arbitrary viewpoint v . We refer to these methods as *regression-based* depth estimation.

In all methods, the estimated depth maps can be further refined using refinement modules [1], [2], [10], [11] and/or progressive reconstruction strategies where the reconstruction is refined every time new images become available (Section 3.1.4).

The subsequent sections will review the state-of-the-art techniques. Within each class of methods, we will first review how the different modules within the common pipeline have been implemented using deep learning techniques. We will then discuss the different methods based on their input and output, the network architecture, the training procedures including the loss functions they use and the degree of supervision they require, and their performances on standard benchmarks.

3 DEPTH BY STEREO MATCHING

Stereo-based depth reconstruction methods take $n > 1$ RGB images and produce a depth map, a disparity map, or an optical flow [12], [13], by matching features across the images. The input images may be captured with calibrated [14] or uncalibrated [15] cameras.

This section focuses on deep learning-based methods that mimic the traditional stereo-matching pipeline, *i.e.*, methods that learn how to explicitly match patches across stereo images for disparity/depth map estimation. We will first review how individual blocks of the stereo-matching pipeline have been implemented using deep learning (Section 3.1), and then discuss how these blocks are put together and trained for depth reconstruction (Section 3.2).

3.1 The pipeline

The stereo-based depth reconstruction process can be formulated as the problem of estimating a map D (D can be a depth/disparity map, or an optical flow) which minimizes an energy function of the form:

$$E(D) = \sum_x C(x, d_x) + \sum_x \sum_{y \in \mathcal{N}_x} E_s(d_x, d_y). \quad (1)$$

Here, x and y are image pixels, $d_x = D(x)$ is the depth / disparity at x , C is a 3D cost volume where $C(x, d_x)$ is the cost of pixel x having depth or disparity equal

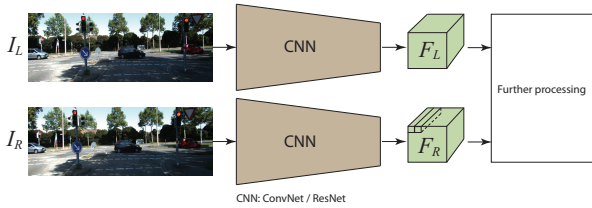


Fig. 1: Feature extraction networks.

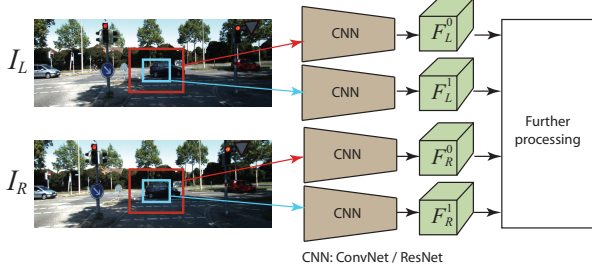


Fig. 2: Multiscale feature extraction networks.

to d_x , \mathcal{N}_x is the set of pixels that are within the neighborhood of x , and E_s is a regularization term, which is used to impose various constraints, *e.g.*, smoothness and left-right depth/disparity consistency, to the final solution. The first term of Equation (1) is the matching cost. In the case of rectified stereo pairs, it measures the cost of matching the pixel $x = (i, j)$ of the left image with the pixel $y = (i, j - d_x)$ of the right image. In the more general multiview stereo case, it measures the inverse likelihood of x on the reference image having depth d_x .

In general, this problem is solved with a pipeline of four building blocks [16]: (1) feature extraction, (2) matching cost calculation and aggregation, (3) disparity/depth calculation, and (4) disparity/depth refinement. The first two blocks construct the cost volume C . The third and fourth blocks define the regularization term and find the depth/disparity map D that minimizes Equation (1). In this section, we review the recent methods that implement these individual blocks using deep learning techniques.

3.1.1 Feature extraction

The first step is to compute a good set of features to match across images. This has been modelled using CNN architectures where the encoder takes either patches around pixels of interests or entire images, and produces dense feature maps in the 2D image space. These features can be of fixed scale (Section 3.1.1.1) or multiscale (Section 3.1.1.2).

3.1.1.1 Fixed-scale features: The main type of network architectures that have been used in the literature is the multi-branch network with shared weights [12], [13], [17], [18], [19], [23], [26], [34], [38], [39], see also Figure 1. It is composed of $n \geq 2$ encoding branches, one for each input image, which act as descriptor computation modules. Each branch

is a Convolutional Neural Networks (CNN), which takes a patch around a pixel i and outputs a feature vector that characterizes that patch [12], [13], [14], [17], [18], [19], [23], [26], [34], [36], [37], [38], [39], [40]. It is generally composed of convolutional layers, spatial normalizations, pooling layers, and rectified linear units (ReLU). The scale of the features that are extracted is controlled by the size of the convolutional filters used in each layer as well as by the number of convolutional and pooling layers. Increasing the size of the filters and/or the number of layers increases the scale of the features that will be extracted. It has also the advantage of capturing more interactions between the image pixels. However, this comes with a high computation cost. To reduce the computational cost while increasing the field of view of the network, some techniques, *e.g.*, [41], use dilated convolutions, *i.e.*, large convolutional filters but with holes and thus they are computationally efficient.

Instead of using fully convolutional networks, some techniques [25] use residual networks, *e.g.*, ResNet [42], *i.e.*, CNNs with residual blocks. A residual block takes an input and estimates the residual that needs to be added to that input. They are used to ease the training of substantially deep networks since learning the residual of a signal is much easier than learning to predict the signal itself. Various types of residual blocks have been used in the literature. For example, Shaked and Wolf [21] proposed appending residual blocks with multilevel connections. Its particularity is that the network learns by itself how to adjust the contribution of the added skip connections.

Table 2 summarises the detailed architecture (number of layers, filter sizes, and stride at each layer) of various methods and the size of the features they produce. Note that, one advantage of convolutional networks is that the convolutional operations within one level are independent from each other, and thus they are parallelizable. As such, all the features of an entire image can be computed with a single forward pass.

3.1.1.2 Multiscale features: The methods described in Section 3.1.1.1 can be extended to extract features at multiple scales, see Figure 2. This is done either by feeding the network with patches of different sizes centered at the same pixel [20], [28], [34], or by using the features computed by the intermediate layers [26]. Note that the deeper is a layer in the network, the larger is the scale of the features it computes.

Liang *et al.* [26] compute multiscale features using a two-layer convolutional network. The output of the two layers are then concatenated and fused, using a convolutional layer, which results in *multi-scale fusion features*. Zagoruyko and Komodakis [34] proposed a central-surround two-stream network which is essentially a network composed of two siamese net-

TABLE 1: Taxonomy of deep learning-based stereo matching algorithms. "Arch." refers to architecture. "CV" refers to cost volume. "corr." refers to correlation.

Method	(1) Feature extraction		(2) Matching cost computation				(3) Cost volume regularization			Depth estimation
	Scale	Arch.	Hand-crafted	Learned similarity		Input	Approach / Net arch.	Output		
				Feature aggregation Pooling, Concatenation	Network FC, CNN				Output Matching score, matching features	
MC-CNN Accr [17], [18]	fixed	CNN	–	concatenation	4 FC layers	matching score	cost volume (CV) CV + features (CVF) CVF + edge map (CVFE)	Standard stereo encoder encoder + decoder	Regularized CV Disparity/depth	argmin, argmax soft argmin, soft argmax subpixel MAP
Luo <i>et al.</i> [19]	fixed	ConvNet	correlation	–	–	matching score	cost volume	Standard stereo	Regularized CV	argmin
Chen <i>et al.</i> [20]	multiscale	ConvNet	corr. + voting	–	–	matching score	cost volume	Standard stereo	Regularized CV	argmin
L-RessMatch [21]	fixed	ResNet	–	concatenation	4 (FC+ReLU) + FC	matching score	cost volume	standard stereo + 4 Conv + 5 FC	Regularized CV	argmin
Han <i>et al.</i> [22]	fixed	ConvNet	–	concatenation	2 (FC + ReLU), FC	matching score	–	–	–	softmax
DispNetCorr [13]	fixed	ConvNet	1D correlation	–	–	matching score	CV + features	encoder + decoder	disparity	–
Pang <i>et al.</i> [23]	fixed	ConvNet	1D correlation	–	–	matching score	CV + features	encoder + decoder	disparity	–
Yu <i>et al.</i> [24]	fixed	ResNet	–	concatenation	encoder+decoder	matching scores	cost volume	3D Conv	Regularized CV	softargmin
Yang <i>et al.</i> [25] (un-sup.)	fixed	ResNet	correlation	–	–	matching scores	CVF + segmentation	encoder-decoder	depth	–
Liang <i>et al.</i> [26]	multiscale	ConvNet	correlation	–	–	matching score	CV + features	encoder-decoder	depth	–
Khamis <i>et al.</i> [27]	fixed	ResNet	L_2	–	–	–	cost volume	encoder	regularized volume	soft argmin/max
Chang & Chen [28] (basic)	multiscale	ResNet	–	concatenate	–	–	cost volume	12 conv layers, residual blocks, upsampling	regularized volume	regression
Chang & Chen [28] (stacked)	multiscale	ResNet	–	concatenation	–	–	cost volume	stacked encoder-decoder blocks, residual connections, upsampling	regularized volume	regression
Zhong <i>et al.</i> [29]	fixed	ResNet	–	concatenation	encoder-decoder	matching scores	cost volume	–	regularized volume	soft argmin
SCM-Net [30]	fixed	ConvNet	–	–	–	matching scores	cost volume	MRF + SCM-Net	regularized volume	–
EdgeStereo [31]	fixed	VGG-16	correlation	–	–	matching scores	CVF + edge map	encoder-decoder (res. pyramid)	depth	–
Ilyakov <i>et al.</i> [32]	fixed	ConvNet	–	concatenation at each disparity	encoder-decoder	matching signatures	matching signatures	encoder + decoder	regularized volume	subpixel MAP
Jie <i>et al.</i> [33]	–	–	–	–	–	–	Left and right CVs	Recurrent ConvLSTM with left-right consistency	disparity	–
Zagoruyko <i>et al.</i> [34]	multiscale	ConvNet	–	concatenation	FC	matching scores	–	–	–	–
Hartmann <i>et al.</i> [35]	fixed	ConvNet	–	Avg pooling	CNN	matching score	–	–	–	softmax
Huang <i>et al.</i> [36]	fixed	ConvNet	–	Max pooling	CNN	matching features	cost volume	encoder	regularized volume	argmin
Yao <i>et al.</i> [37]	fixed	ConvNet	–	Var. pooling	CNN	matching features	cost volume	encoder-decoder	regularized volume	softmax
Hynn <i>et al.</i> [14]	fixed	2D Conv	–	Conv across depth layers	CNN	matching score	cost volume	encoder	regularized volume	soft argmin/max
Kar <i>et al.</i> [38]	fixed	ConvNet	–	feature unprojection + recurrent fusion	CNN	matching score	cost volume	encoder-decoder	3D occupancy grid	projection
Kendall <i>et al.</i> [39]	fixed	ConvNet	–	concatenation	CNN	matching features	cost volume	encoder-decoder	regularized volume	soft argmin/max

TABLE 2: Network architectures for feature extraction. Each layer of the network is described in the following format: (filter size, type, stride, output feature size, scaling). Scaling refers to upscaling or downscaling of the resolution of the output with respect to the input. SPP refers to Spatial Pyramid Pooling. The last column refers to the feature size as produced by the last layer.

Method	Input	Type	Architecture	Feature size
Dosovitskiy <i>et al.</i> [12]	512×384	CNN	$(7 \times 7, conv, 2, 64, -), (5 \times 5, conv, 2, 128, -), (5 \times 5, conv, 2, 256, -)$	$64 \times 48 \times 256$
Chen <i>et al.</i> [20]	13×13	CNN	$(3 \times 3, conv, -, 32, -)_{1,2}, (5 \times 5, conv, -, 200, -)_{3,4}$	1×200
Zagoruyko [34]	patches of varying sizes	CNN + SPP	$(-, conv + ReLU, -, -, -)_{1,2}, (-, conv + SPP, -, -, -)$	$1 \times c$
Zbontar & LeCun [18] (fast)	patches 9×9	CNN	$(3 \times 3, conv + ReLU, -, 64, -)_{1,2,3}, (3 \times 3, conv, -, 64, -)$	1×64
Zbontar & LeCun [18] (accr)	patches 9×9	CNN	$(3 \times 3, conv + ReLU, -, 112, -)_{1,2,3}, (3 \times 3, conv, -, 112, -)$	1×112
Luo <i>et al.</i> [19]	Small patch	CNN	$(3 \times 3 \text{ or } 5 \times 5, conv + ReLU, -, 32 \text{ or } 64, -)_{1,2,3}, \text{ or } (5 \times 5, conv, -, 32 \text{ or } 64, -)$	$1 \times 32 \text{ or } 1 \times 64$
DispNetC [13], Pang <i>et al.</i> [23]	768×364	CNN	$(7 \times 7, conv, 2, 64, -), (5 \times 5, conv, 2, 128, -)$	$192 \times 96 \times 128$
Kendall <i>et al.</i> [39]	$H \times W$	CNN (2D conv) + Residual connections	$(5 \times 5, conv, 2, 32, /2), [(3 \times 3, conv, -, 32, -), (3 \times 3, res, -, 32, -)]_{1,\dots,7}, (3 \times 3, conv, -, 32, -)$, No ReLU or BN on the last layer	$\frac{1}{2}H \times \frac{1}{2}W \times 32$
Liang <i>et al.</i> [26]	$H \times W$	CNN	$(7 \times 7, conv, 2, 64, /2), (5 \times 5, conv, 2, 128, /2)$	$\frac{1}{4}H \times \frac{1}{4}W \times 128$
Kar <i>et al.</i> [38]	224×224	CNN	$(3 \times 3, conv, -, 64, -), (3 \times 3, conv, -, 64, -), (2 \times 2, maxpool, -, 64, -)$ $(3 \times 3, conv, -, 128, -), (3 \times 3, conv, -, 128, -), (2 \times 2, maxpool, -, 128, -)$ $(3 \times 3, conv, -, 512, -), (3 \times 3, conv, -, 512, -), (2 \times 2, maxpool, -, 512, -)$ $(3 \times 3, conv, -, 1024, -), (3 \times 3, conv, -, 1024, -)$	$32 \times 32 \times 1024$
Yang <i>et al.</i> [25]	$H \times W$	CNN + Residual blocks	$(3 \times 3, conv, 2, 64, /2), (3 \times 3, conv, 1, 64, /1), (3 \times 3, conv, 1, 128, /1)$ $(3 \times 3, maxpool, 2, 128, /2), (3 \times 3, res_block, 1, 256, /2)$ $(3 \times 3, res_block, 1, 256, /1)_{1,2}, (3 \times 3, res_block, 1, 512, /2)$	–
Shaked and Wolf [21]	11×11	CNN + Outer λ -residual blocks	$conv_1, ReLU$, Outer λ - residual block, $ReLU, conv_{2\dots 5}, ReLU$, Outer λ - residual block	$1 \times 1 \times 112$

works combined at the output by a top network. The first siamese network, called central high-resolution stream, receives as input two 32×32 patches that are generated by cropping (at the original resolution) the central 32×32 part of each 64×64 -input patch. The second network, called surround low-resolution stream, receives as input two 32×32 patches generated by downsampling at half the original input. Chen *et al.* [20] also used a similar approach but each network processes patches of size 13×13 . The main advantage of this architecture is that it can compute the features at two different resolutions in a single forward pass. It, however, requires one stream by scale, which is not practical if more than two scales are needed.

Chang and Chen [28] used Spatial Pyramid Pooling (SPP) module to aggregate context in different scales

and location. More precisely, the feature extraction module is composed of a CNN of seven layers, and an SPP module followed by convolutional layers. The CNN produces a feature map of size $\frac{1}{4}H \times \frac{1}{4}W \times 128$. The SPP module then takes a patch around each pixel but at four different sizes ($8 \times 8 \times 128$, $16 \times 16 \times 128$, $32 \times 32 \times 128$, and $64 \times 64 \times 128$), and converts them into one-channel by mean pooling followed by a 1×1 convolution. These are then upsampled to the desired size and concatenated with features from different layers of the CNN, and further processed with additional convolutional layers to produce the features that will be fed to the subsequent modules for matching and disparity computation. Chang and Chen [28] showed that the SPP module enables estimating disparity for inherently ill-posed regions.

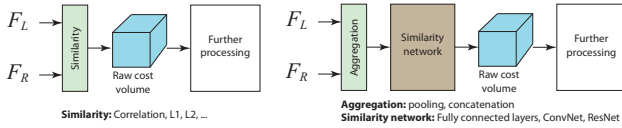


Fig. 3: Taxonomy of similarity computation networks.

In general, Spatial Pyramid Pooling (SPP) are convenient for processing patches of arbitrary sizes. For instance, Zaogoruyko and Komodakis [34] append an SPP layer at the end of the feature computation network. Such a layer aggregates the features of the last convolutional layer through spatial pooling, where the size of the pooling regions depends on the size of the input. By doing so, one will be able to feed the network with patches of arbitrary sizes and compute feature vectors of the same dimension.

3.1.2 Matching cost computation

This module takes the features computed on each of the input images, and computes the matching scores of Equation (1). The matching scores form a 3D volume, called *Disparity Space Image (DSI)* [16], of the form $C(x, d_x)$ where $x = (i, j)$ is the image coordinates of pixel x and $d_x \in [0, n_d]$ is the candidate disparity/depth value. It is of size $\bar{W} \times \bar{H} \times (n_d + 1)$, where $\bar{W} \times \bar{H}$ is the resolution at which we want to compute the depth map and n_d is the number of depth/disparity values. In stereo matching, if the left and right images have been rectified so that the epipolar lines are horizontal then $C(x, d_x)$ is the similarity between the pixel $x = (i, j)$ on the rectified left image and the pixel $y = (i, j - d_x)$ on the rectified right image. Otherwise, $C(x, d_x)$ indicates the likelihood, or probability, of the pixel x having depth d_x .

Similar to traditional stereo-matching methods [16], the cost volume is computed by comparing the deep features of the input images using standard metrics such as the L_2 distance, the cosine distance, and the (normalized) correlation distance (Section 3.1.2.1). With the advent of deep neural networks, several new mechanisms have been proposed (Section 3.1.2.2). Figure 3 shows the main similarity computation architectures. Below, we discuss them in details.

3.1.2.1 Using distance measures: The simplest way to form a cost volume is by taking the distance between the feature vector of a pixel and the feature vectors of the matching candidates, *i.e.*, the pixels on the other image that are within a pre-defined disparity range. There are several distance measures that can be used. Khamis *et al.* [27], for example, used the L_2 distance. Other techniques, *e.g.*, [12], [13], [18], [19], [20], [26], used correlation, *i.e.*, the inner product between feature vectors. The main advantage of correlation over the L_2 distance is that it can be implemented using a layer of 2D [12] or 1D [13] convolutional operations, called correlation layer. 1D

correlations are computationally more efficient than their 2D counterpart. They, however, require rectified images so that the search for correspondences is restricted to pixels within the same row.

Compared to the two other methods that will be described below, the main advantage of the correlation layer is that it does not require training since the filters are in fact the features computed by the second branch of the network.

3.1.2.2 Using similarity-learning networks:

These methods aggregate the features produced by the different branches, and process them with a top network, which produces a matching score. The rationale is to let the network learn from data the appropriate similarity measure.

(1) Feature aggregation. Some stereo reconstruction methods first aggregate the features computed by the different branches of the network before passing them through further processing layers. The aggregation can be done in two different ways:

Aggregation by concatenation. The simplest way is to just concatenate the learned features computed by the different branches of the network and feed them to the similarity computation network [17], [18], [34], [39]. Kendall *et al.* [39] concatenate each feature with their corresponding feature from the opposite stereo image across each disparity level, and pack these into a 4D volume of dimensionality $H \times W \times (n_d + 1) \times c$ (c here is the dimension of the features). Huang *et al.* [36], on the other hand, concatenate the 64^3 feature volume, computed for the $64 \times 64 \times 3$ reference image, and another volume of the same size from the plane-sweep volume plane that corresponds to the n -th input image at the d -th disparity level, to form a $64 \times 64 \times 128$ volume. Zhong *et al.* [29] followed the same approach but concatenate the features in an interleaved manner. That is, if \mathbf{f}_L is the feature map of the left image and \mathbf{f}_R the feature map of the right image then the final feature volume is assembled in such a way that its $2i$ -th slice holds the left feature map while the $(2i + 1)$ -th slice holds the right feature map but at disparity $d = i$. That is,

$$\mathbf{f}_{LR}(u, v, d) = \mathbf{f}_L(u, v) \parallel \mathbf{f}_R(u - d, v), \quad (2)$$

where \parallel denotes the vector concatenation.

Aggregation by pooling. Another approach is to use pooling layers to aggregate the feature maps. For instance, Hartmann *et al.* [35] used average pooling. Huang *et al.* [36] used max-pooling, while Yao *et al.* [37] take their variance, which is equivalent to first computing the average feature vector and then taking the average distance of the other features to the mean.

The main advantage of pooling over concatenation is three-fold; First, it does not increase the dimensionality of the data that is fed to the top similarity computation network, which facilitates the training.

Second, it makes it possible to input a varying number of views without retraining the network. This is particularly suitable for multiview stereo (MVS) approaches, especially when dealing with an arbitrary number of input images and when the number of images at runtime may be different from the number of images at training. Finally, pooling ensures that the results are invariant with respect to the order in which the images are fed to the network.

(2) Similarity computation. There are two types of networks that have been used in the literature: fully connected networks and convolutional networks.

Using fully-connected networks. In these methods, the similarity computation network is composed of fully connected layers [17], [18], [34]. The last layer produces the probability of the input feature vectors being a good or a bad match. Zagoruyko and Komodakis [34], for example, used a network composed of two fully connected layers (each with 512 hidden units) that are separated by a ReLU activation layer. Zbontar and LeCun [17], [18] used five fully connected layers with 300 neurones each except for the last layer, which projects the output to two real numbers that are fed through a softmax function, which in turn produces the probability of the two input feature vectors being a good match.

Using convolutional networks. Another approach is to aggregate the features and further post-process them using convolutional networks, which output either matching scores [14], [35], [38] (similar to correlation layers), or matching features [36], [39]. The most commonly used CNNs include max-pooling layers, which provide invariance in spatial transformation. Pooling layers also widen the receptive field area of a CNN without increasing the number of parameters. The drawback is that the network loses fine details. To overcome this limitation, Park and Lee [43] introduced a pixel-wise pyramid pooling layer to enlarge the receptive field during the comparison of two input patches. This method produced more accurate matching cost than [17].

One limitation of correlation layers and convolutional networks that produce a single cost value is that they decimate the feature dimension. Thus, they restrict the network to only learning relative representations between features, and cannot carry absolute feature representations. Instead, a matching feature can be seen as a descriptor, or a feature vector, that characterizes the similarity between two given patches. The simplest way of computing matching features is by aggregating the feature maps produced by the descriptor computation branches of the network [39], [44], or by using an encoder that takes the concatenated features and produces another volume of matching features [36]. For instance, Huang *et al.* [36] take the $64 \times 64 \times 128$ volume, formed

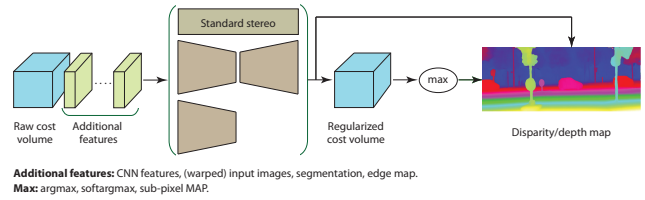


Fig. 4: Cost volume regularization and disparity/depth map estimation.

by features, and process it using three convolutional layers to produce a $64 \times 64 \times 4$ volume of matching features. Since the approach computes $n_d + 1$ matching features, one for each disparity level ($n_d = 100$ in [36]), these need to be aggregated into a single matching feature. This is done using another encoder-decoder network with skip connections [36]. Each level of the encoder is formed by a stride-2 convolution layer followed by an ordinary convolution layer. Each level of the decoder is formed by two convolution layers followed by a bilinear upsampling layer. It produces a volume of matching features of size $64 \times 64 \times 800$.

(3) Cost volume aggregation. In general, multiview stereo methods, which take n input images, compute $n - 1$ cost or feature matching volumes, one for each pair (I_0, I_i) , where I_0 is the reference image. These need to be aggregated into a single cost/feature matching volume before feeding it into the disparity/depth calculation module. This has been done either by using (max, average) pooling or pooling followed by an encoder [36], [37], which produces the final cost/feature matching volume C .

3.1.3 Disparity and depth computation

We have seen so far the various deep learning techniques that have been used to estimate the cost volume C , *i.e.*, the first term of Equation (1). The goal now is to estimate the depth/disparity map \hat{D} that minimizes the energy function $E(D)$ of Equation (1). This is done in two steps; (1) cost volume regularization, and (2) disparity/depth estimation from the regularized cost volume.

3.1.3.1 Cost volume regularization: Once a raw cost volume is estimated, one can estimate disparity/depth by dropping the smoothness term of Equation (1) and taking the argmin, the softmax, or the subpixel MAP approximation (see Section 3.1.3.2). In general, however, the raw cost volume computed from image features could be noise-contaminated (*e.g.*, due to the existence of non-Lambertian surfaces, object occlusions, and repetitive patterns). Thus, the estimated depth maps can be noisy.

Several deep learning-based regularization techniques have been proposed to estimate accurate depth maps from the cost volume, see Figure 4 for an illustration of the taxonomy. Their input can be the

cost volume [14], [27], [28], [29], [36], [37], [38], [39], the cost volume concatenated with the features of the reference image [12], [26] and/or with semantic features such as the segmentation mask [25] or the edge map [31]. The produced volume is then processed with either an encoder-decoder network with skip connections [12], [25], [26], [28], [29], [31], [37], [38], [39], or just an encoder [14], [27], [36], to produce either a regularized cost volume [14], [27], [28], [29], [36], [37], [38], [39], or directly the disparity/depth map [12], [25], [26], [31]. In the former case, the regularized volume is processed using argmin, softargmin, or subpixel MAP approximation (Section 3.1.3.2) to produce the final disparity/depth map.

Note that some methods adopt an MRF-based stereo framework for cost volume regularization [17], [19], [20]. In these methods, the initial cost volume C is fed to a global [16] or a semi-global [45] matcher to compute the disparity map. Semi-global methods define the smoothness term as

$$E_s(d_x, d_y) = \alpha_1 \delta(|d_x - d_y| = 1) + \alpha_2 \delta(|d_x - d_y| > 1), \quad (3)$$

where α_1 and α_2 are positive weights chosen such that $\alpha_2 > \alpha_1$. Instead of manually setting these two parameters, Seki *et al.* [30] proposed SGM-Net, a neural network trained to provide these parameters at each image pixel. They obtained better penalties than hand-tuned methods as in [17].

3.1.3.2 Disparity/depth estimation: The simplest way to estimate disparity/depth from the (regularized) cost volume C is by using the pixel-wise argmin, *i.e.*, $d_x = \arg \min_d C(x, d)$ (or equivalently argmax if the volume C encodes likelihood) [36]. However, the agrmin/argmax operator is unable to produce sub-pixel accuracy and cannot be trained with back-propagation due to its non-differentiability. Another approach is to process the cost volume using a layer of per-pixel softmin, also called soft argmin (or equivalently softmax), over disparity/depth [14], [27], [39]:

$$d^* = \frac{1}{\sum_{j=0}^{n_d} e^{-C(x,j)}} \sum_{d=0}^{n_d} d \times e^{-C(x,d)}. \quad (4)$$

It approximates sub-pixel MAP solution when the distribution is unimodal and symmetric [32]. When this assumption is not fulfilled, the softargmin blends the modes and may produce a solution that is far from all the modes. Also, the network only learns for the disparity range used during training. If the disparity range changes at runtime, then the network needs to be re-trained. To address these issues, Tulyakov *et al.* [32] introduced the sub-pixel MAP approximation that computes a weighted mean around the disparity with maximum posterior probability as:

$$d^* = \sum_{d:|\hat{d}-d|\leq\delta} d \cdot \sigma(C(x,d)), \quad (5)$$

where δ is a meta parameter set to 4 in [32], and $\hat{d} = \arg \max_d C(x, d)$. Note that, in Tulyakov *et al.* [32], the sub-pixel MAP is only used for inference.

3.1.4 Refinement

In general, the predicted disparity/depth maps are of low resolution, miss fine details, and may suffer from over-smoothing especially at object boundaries. Some methods also output incomplete and/or sparse maps. Deep-learning networks that directly predict high resolution and high quality maps would require a large number of parameters and thus are usually difficult to train. Instead, an additional refinement block is added to the pipeline. Its goal is to (1) improve the resolution of the estimated disparity/depth map, (2) refine the reconstruction of the fine details, and (3) perform depth/disparity completion. Such refinement block can be implemented using traditional approaches. For instance, Dosovitskiy *et al.* [12] use the variational approach from [54]. Huang *et al.* [36] apply the Fully-Connected Conditional Random Field (DenseCRF) of [55] to the predicted raw disparities. Li *et al.* [1] refine the predicted depth (or surface normals) from the super-pixel level to pixel level using a hierarchical Conditional Random Field (CRF). The use of DenseCRF or hierarchical CRF encourages the pixels that are spatially close and with similar colors to have closer disparity predictions. Also, this step removes unreliable matches via left-right check. Chen *et al.* [20] compute the final disparity map from the raw one, after removing unreliable matches, by propagating reliable disparities to non-reliable areas [56]. Note that the use of CRF for depth estimation has been also explored by Liu *et al.* [4]. However, unlike Li *et al.* [1], Liu *et al.* [4] used a CNN to minimize the CRF energy.

In this section, we will look at how the refinement block has been implemented using deep learning, see Table 3 for a taxonomy of these methods. In general, the input to the refinement module can be: (1) the estimated depth/disparity map, (2) the estimated depth/disparity map concatenated with the reference image scaled to the resolution of the estimated depth/disparity map [37], (3) the initially-estimated disparity map, the cost volume, and the reconstruction error, which is calculated as the absolute difference between the multi-scale fusion features of the left image and the multi-scale fusion features of the right image but back-warped using the initial disparity map to the left image [26], (4) the raw disparity/depth map, and the right image but warped into the view of the left image using the estimated initial disparity map [52], and (5) the estimated depth/disparity map concatenated with the feature map of the reference image, *e.g.*, the output of a first convolutional layer [10].

Note that refinement can be hierarchical by cascading several refinement modules [23], [49].

TABLE 3: Taxonomy of disparity/depth refinement techniques. "reco error": reconstruction error. "CSPN": Convolutional Spatial Propagation Networks.

Traditional methods	Deep learning-based methods				
	Input	Approach			Other cues
		Bottom-up	Top-down	Guided	
Variational [12]	Raw depth	Split and merge [46]	Decoder [10]	Detect - Replace - Refine [47]	Joint depth and normal [48]
Fully-connected CRF [36]	Depth + Ref. Image [37]	Sliding window [11]	Encoder + decoder [15], [27], [49]	Depth-balanced loss [46]	Left-Right consistency [33]
Hierarchical CRF [1]	Depth + CV + Ref. Image + rec. error [26]	Diffusion using CSPN [50]	Encoder + decoder with residual learning [23], [26], [37], [49], [51]		
Depth propagation [20]	Depth + Rewarped right image [52]	Diffusion using recurrent convolutional operation [53]	Progressive upsampling [51]		
CRF energy minimized with CNN [4]	Depth + Learned features [10].				

3.1.4.1 Bottom-up approaches: A bottom-up network operates in a sliding window-like approach. It takes small patches and estimates the refined depth at the center of the patch [11]. Lee *et al.* [46] follow a split-and-merge approach. The input image is split into regions, and a depth is estimated for each region. The estimates are then merged using a fusion network, which operates in the Fourier domain so that depth maps with different cropping ratios can be handled. The rationale is that inferring accurate depth at the desired resolution would require large networks with a large number of parameters to estimate. By making the network focus on small regions, fine details can be recovered with less parameters. However, obtaining the entire refined map will require multiple forward passes, which is not suitable for realtime applications.

Another bottom-up refinement strategy is based on diffusion processes. The idea is to start with an incomplete depth map and use anisotropic diffusion to propagate the known depth to the regions where depth is missing. Convolutional Spatial Propagation Networks (CSPN) [50], which implement an anisotropic diffusion process, are particularly suitable for this task. They take as input the original image and a sparse depth map, which can be the output of a depth estimation network, and predict, using a deep CNN, the diffusion tensor. This is then applied to the initial map to obtain the refined one. Cheng *et al.* [53] used this approach in their proposed refinement module. It takes an initial depth estimate and performs linear propagation, in which the propagation is performed with a manner of recurrent convolutional operation, and the affinity among neighboring pixels is learned through a deep CNN.

3.1.4.2 Top-down approaches: Another approach is to use a top-down network that processes the entire raw disparity/depth map. It can be implemented as (1) a decoder, which consists of unpooling units to extend the resolution of its input, as opposed to pooling, and convolution layers [10], or with (2) an encoder-decoder network [15]. In the latter case, the encoder is to map the input into a latent

space. The decoder then predicts the high resolution map from the latent variable. These networks also use skip connections from the contracting part to the expanding part so that fine details can be preserved. To avoid the checkboard artifacts produced by the deconvolutions and upconvolutions [27], [49], [57], several papers first upsample the initial map, *e.g.*, using bilinear upsampling, and then apply convolutions [27], [49].

These architectures can be used to directly predict the high resolution maps but also to predict the residuals [26], [37], [49]. As opposed to directly learning the refined disparity map, residual learning provides a more effective refinement. In this approach, the estimated map and the resized reference image are concatenated and used as a 4-channel input to a refinement network, which learns the disparity/depth residual. The estimated residual is then added to the originally estimated map to generate the refined map.

Pang *et al.* [23] refine the raW disparity map using a cascade of two CNNs. The first stage advances the DispNet of [13] by adding extra up-convolution modules, leading to disparity images with more details. The second stage, initialized by the output of the first stage, explicitly rectifies the disparity; it couples with the first-stage and generates residual signals across multiple scales. The summation of the outputs from the two stages gives the final disparity.

Jeon and Lee [51] proposed a deep Laplacian Pyramid Network to spatially varying noise and holes. By considering local and global contexts, the network progressively reduces the noise and fills the holes from coarse to fine scales. It first predicts, using residual learning, a clean complete depth image at a coarse scale (quarter of the original resolution). The prediction is then progressively upsampled through the pyramid to predict the half and original sized clean depth image. The network is trained with 3D supervision using a loss that is a combination of a data loss and a structure-preserving loss. The data loss is a weighted sum of L_1 distance between the ground-truth depth and the estimated depth, the L_1 distance between the gradient of the ground-truth depth and the estimated depth, and the L_1 distance

between the normal vectors of the estimated and ground-truth depths. The structure-preserving loss is gradient-based to preserve the original structures and discontinuities. It is defined as the L_2 distance between the maximum gradient around a pixel in the ground-truth depth map and the maximum gradient around that pixel in the estimate depth map.

3.1.4.3 Guided refinement: Gidaris and Komodakis [47] argue that the approaches that predict either new depth estimates or residual corrections are sub-optimal. Instead, they propose a generic CNN architecture that decomposes the refinement task into three steps: (1) detecting the incorrect initial estimates, (2) replacing the incorrect labels with new ones, and (3) refining the renewed labels by predicting residual corrections with respect to them. Since the approach is generic, it can be used to refine the raw depth map produced by any other method, *e.g.*, [19].

In general, the predictions of the baseline backbone, which is composed of an encoder-decoder, are coarse and smooth due to the lack of depth details. To overcome this, Zhang *et al.* [58] introduced a hierarchical guidance strategy, which guides the estimation process to predict fine-grained details. They perform this by attaching refinement networks (composed of 5 conv-residual blocks and several following 1×1 convolution layers) to the last three layers of the encoder (one per layer). Its role is to predict depth maps at these levels. The features learned by these refinement networks are used as input to their corresponding layers on the decoder part of the backbone network. This is similar to using skip connection. However, instead of feeding directly the features of the encoder, these are further processed to predict depth map at that level.

Finally, to handle equally close and far depths, Li *et al.* [46] introduced depth-balanced Euclidean loss to reliably train the network on a wide range of depths.

3.1.4.4 Leveraging other cues: Qi *et al.* [48] proposed a mechanism that uses the depth map to refine the quality of the normal estimates, and the normal map to refine the quality of the depth estimates. This is done using a two-stream CNN, one for estimating an initial depth map and another for estimating an initial normal map. Then, it uses another two-stream networks: a depth-to-normal network and a normal-to-depth network. The former is used to refine the normal map using the initial depth map. The latter is used to refine the depth map using the estimated normal map.

- The depth-to-normal network first takes the initial depth map and generates a rough normal map using PCA analysis. This is then fed into a 3-layer CNN, which estimates the residual. The residual is then added to the rough normal map, concatenated with the initial raw normal map, and further processed with one convolutional

layer to output the refined normal map.

- The normal-to-depth network uses kernel regression process, which takes the initial normal and depth maps, and regresses the refined depth map.

Instead of estimating a single depth map from the reference image, one can estimate multiple depth maps, one per input image, check the consistency of the estimates, and use the consistency maps to (recursively) refine the estimates. In the case of stereo matching, this process is referred to as the left-right consistency check, which traditionally was an isolated post-processing step and heavily hand-crafted.

The standard approach for implementing the left-right consistency check is as follows;

- Compute two disparity maps D_l and D_r , one for the left image and another for the right image.
- Reproject the right disparity map onto the coordinates of the left image, obtaining \hat{D}_r .
- Compute the error or confidence map indicating whether the estimated disparity is correct or not.
- Finally, use the computed confidence map to refine the disparity estimate.

A simple way of computing the confidence map is by taking pixel-wise difference. Seki *et al.* [59], on the other hand, used a CNN trained in a classifier manner. It outputs a label per pixel indicating whether the estimated disparity is correct or not. This confidence map is then incorporated into a Semi-Global Matching (SGM) for dense disparity estimation.

Jie *et al.* [33] perform left-right consistency check jointly with disparity estimation, using a Left-Right Comparative Recurrent (LRRCR) model. It consists of two parallelly stacked convolutional LSTM networks. The left network takes the cost volume and generates a disparity map for the left image. Similarly, the right network generates, independently of the left network, a disparity map for the right image. The two maps are converted to the opposite coordinates (using the known camera parameters) for comparison with each other. Such comparison produces two error maps, one for the left disparity and another for the right disparity. Finally, the error map for each image is concatenated with its associated cost volume and used as input at the next step to the convolutional LSTM. This will allow the LRRCR model to selectively focus on the left-right mismatched regions at the next step.

3.2 Stereo matching networks

In the previous section, we have discussed how the different blocks of the stereo matching pipeline have been implemented using deep learning. This section discusses how different state-of-the-art techniques used these blocks and put them together to solve the pairwise stereo matching-based depth reconstruction problem.

3.2.1 Early methods

Early methods, *e.g.*, [17], [19], [20], [22], [34], [60], replace the hand-crafted features and similarity computation with deep learning architectures. The basic architecture is composed of a stack of the modules described in Section 3.1. The feature extraction module is implemented as a multi-branch network, with shared weights. Each branch computes features from its input. These are then matched using:

- a fixed correlation layer (implemented as a convolutional layer) [17], [19],
- a fully connected neural network [18], [21], [22], [34], which takes as input the concatenated features of the patches from the left and right images and produces a matching score.
- convolutional networks composed of convolutional layers followed by ReLU [35].

Using convolutional and/or fully-connected layers enables the network to learn from data the appropriate similarity measure, instead of imposing one at the outset. It is more accurate than using a correlation layer but is significantly slower.

Note that while Zbontar *et al.* [17], [18] and Han *et al.* [22] use standard convolutional layers in the feature extraction block, Shaked and Wolf [21] add residual blocks with multilevel weighted residual connections to facilitate the training of very deep networks. It was demonstrated that this architecture outperformed the base network of Zbontar *et al.* [17]. To enable multiscale features, Chen *et al.* [20] replicate twice the feature extraction module and the correlation layer. The two instances take patches around the same pixel but of different sizes, and produce two matching scores. These are then merged using voting. Chen *et al.*'s approach shares some similarities with the central-surround two-stream network of [34]. The main difference is that in [34], the output of the four branches of the descriptor computation module is given as input to a top decision network for fusion and similarity computation, instead of using voting. Zagoruyko and Komodakis [34] add at the end of each feature computation branch a Spatial Pyramid Pooling so that patches of arbitrary sizes can be compared.

Using these approaches, inferring the raw cost volume from a pair of stereo images is performed using a moving window-like approach, which would require multiple forward passes (n_d forward passes per pixel). However, since correlations are highly parallelizable, the number of forward passes can be significantly reduced. For instance, Luo *et al.* [19] reduce the number of forward passes to one pass per pixel by using a siamese network where the first branch takes a patch around a pixel while the second branch takes a larger patch that expands over all possible disparities. The output is a single 64D representation for the left branch, and $n_d \times 64$ for the right branch. A correlation layer then computes a vector of length n_d where its

d -th element is the cost of matching the pixel x on the left image with the pixel $x-d$ on the rectified right image. Other papers, *e.g.*, [21], [25], [27], [29], [35], [39], [49], compute the feature maps of the left and right images in a single forward pass. These, however, have a high memory footprint at runtime and thus the feature map is usually computed at a resolution that is lower than the resolution of the input images.

These early methods produce matching scores that can be aggregated into a cost volume, which corresponds to the data term of Equation (1). They then extensively rely on hand-engineered post-processing steps, which are not jointly trained with the feature computation and feature matching networks, to regularize the cost volume and refine the disparity/depth estimation [18], [19], [20], [30].

3.2.2 End-to-end methods

Recent works solve the stereo matching problem using a pipeline that is trained end-to-end without post-processing. For instance, Knöbelreiter *et al.* [61] proposed a hybrid CNN-CRF. The CNN part computes the matching term of Equation (1). This then becomes the unary term of a Conditional Random Field (CRF) module, which performs the regularization. The pairwise term of the CRF is parameterized by edge weights and is computed using another CNN. Using the learned unary and pairwise costs, the CRF tries to find a joint solution optimizing the total sum of all unary and pairwise costs in a 4-connected graph. The whole CNN-CRF hybrid pipeline, which is trained end-to-end, could achieve a competitive performance using much fewer parameters (and thus a better utilization of the training data) than the earlier methods.

Others papers [12], [13], [21], [25], [27], [29], [35], [39], [49] implement the entire pipeline using convolutional networks. In these approaches, the cost volume is computed in a single forward pass, which results in a high memory footprint. To reduce the memory footprint, some methods such as [12], [13] compute a lower resolution raw cost volume, *e.g.*, one half or one fourth of the size of the input images. Some methods, *e.g.*, [21], [28], [29], [39], omit the matching module. The left-right features, concatenated across the disparity range, are directly fed to the regularization and depth computation module. This, however, results in even larger memory footprint. Tulyakov *et al.* [32] reduce the memory use, without sacrificing accuracy, by introducing a matching module that compresses the concatenated features into compact matching signatures. The approach uses mean pooling instead of feature concatenation. This also reduces the memory footprint. More importantly, it allows the network to handle arbitrary number of multiview images, and to vary the number of input at runtime without re-training the network. Note that pooling layers have been used to aggregate features of different scales [28].

The regularization module takes the cost volume, the concatenated features, or the cost volume concatenated with the reference image [12], with the features of the reference image [12], [26], and/or with semantic features such as the segmentation mask [25] or the edge map [31], which serve as semantic priors. It then regularizes it and outputs either a depth/disparity map [12], [13], [23], [26], [31] or a distribution over depth/disparities [28], [29], [33], [39]. Both the segmentation mask [25] and the edge map [31] can be computed using deep networks that are trained jointly and end-to-end with the disparity/depth estimation networks. Appending semantic features to the cost volume improves the reconstruction of fine details, especially near object boundaries.

The regularization module is usually implemented as convolution-deconvolution (hourglass) deep network with skip connections between the contracting and expanding parts [12], [13], [23], [26], [28], [29], [39], or as a convolutional network [14], [27]. It can use 2D convolutions [12], [13], [23], [26] or 3D convolutions [28], [29], [33], [39]. The latter has less parameters. In both cases, their disparity range is fixed in advance and cannot be re-adjusted without re-training. Tulyakov *et al.* [32] introduced the sub-pixel MAP approximation for inference, which computes a weighted mean around the disparity with MAP probability. They showed that it is more robust to erroneous modes in the distribution and allows to modify the disparity range without re-training.

Depth can be computed from the regularized cost volume using (1) the softargmin operator [14], [27], [39], [49], which is differentiable and allows sub-pixel accuracy but limited to network outputs that are unimodal, or (2) sub-pixel MAP approximation [32], which can handle multi-modal distributions.

Some papers, *e.g.*, [39], directly regress high-resolution map without an explicit refinement module. This is done by adding a final upconvoluntal layer to the regression module in order to upscale the cost volume to the resolution of the input images. In general, however, inferring high resolution depth maps would require large networks, which are expensive in terms of memory storage but also hard to train given the large number of free parameters. As such, some methods first estimate a low-resolution depth map and then refine it using a refinement module [23], [26], [33]. The refinement module as well as the early modules are trained jointly and end-to-end.

3.3 Multiview stereo (MVS) matching networks

The methods described in Section 3.2 have been designed to reconstruct depth/disparity maps from a pair of stereo images. These methods can be extended to the multiview stereo (MVS) case, *i.e.*, $n > 2$, by replicating the feature computation branch n times. The features computed by the different branches can

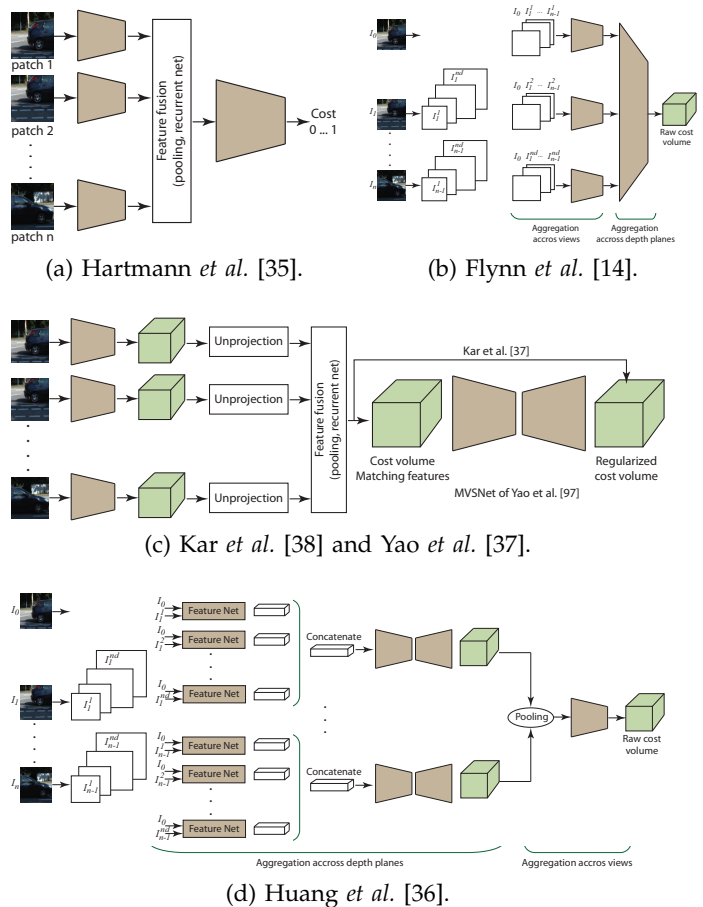


Fig. 5: Taxonomy of multiviewstereo methods. (a), (b), and (c) perform early fusion, while (d) performs early fusion by aggregating features across depth planes, and late fusion by aggregating cost volumes across views.

then be aggregated using, for example, pooling [35], [36], [37] or a recurrent fusion unit [38] before feeding the aggregated features into a top network, which regresses the depth map (Figures 5-(a), (b), and (c)). Alternatively, one can sample pairs of views, estimate the cost volume from each pair, and then merge the cost volumes either by voting or pooling [36] (Figure 5-(d)). The former called *early fusion* while the latter is called *late fusion*.

The early work of Hartmann *et al.* [35] introduced a mechanism to learn multi-patch similarity, which replaces the correlation layer used in stereo matching. The approach uses pooling to aggregate the features computed on the different patches before feeding them to the subsequent blocks of the standard stereo matching pipeline. Recent techniques use Plane-Sweep Volumes (PSV) [14], [36], feature unprojection to the 3D space [37], [38], and image unprojection to the 3D space resulting in the Colored Voxel Cube (CVC) [62].

Flynn *et al.* [14] and Huang *et al.* [36] use the camera parameters to unproject the input images into Plane-Sweep Volumes (PSV) and feed them into the

subsequent feature extraction and feature matching networks. Flynn *et al.* [14]’s network is composed of n_d branches, one for each depth plane (or depth value). The d -th branch of the network takes as input the reference image and the planes of the Plane-Sweep Volumes of the other images and which are located at depth d . These are packed together and fed to a two-stages network. The first stage, which consists of 2D convolutional rectified linear layers that share weights across all depth planes, computes matching features between the reference image and the PSV planes located at depth d . The second stage is composed of convolutional layers that are connected across depth planes in order to model interactions between them. The final layer of the network is a per-pixel softmax over depth, which returns the most probable depth value per pixel. The approach, which has been used for pairwise and multiview stereo matching, requires that the number of views and the camera parameters of each view to be known. It also requires setting in advance the disparity range.

Huang *et al.* [36]’s approach, which also operates on the plane-sweep volumes, uses a network composed of three parts: the patch matching part, the intra-volume feature aggregation part, and the inter-volume feature aggregation part:

- The patch matching part is a siamese network. Its first branch extracts features from a patch in the reference image and the second one from the plane-sweep volume that corresponds to the i -th input image at the d -th disparity level. (100 disparity values have been used.) The features are then concatenated and passed to the subsequent convolutional layers. This process is repeated for all the plane-swept images.
- The output from the patch matching module of the d -th plane-sweep volume are concatenated and fed into another encoder-decoder which produces a feature vector F_d of size $64 \times 64 \times 800$.
- All the feature vectors $F_i, i = 1, \dots, n$ (one for each input image), are aggregated using a max-pooling layer followed by convolutional layers, which produce a depth map of size 64×64 .

Unlike Flynn *et al.* [14], Huang *et al.* [36]’s approach does not require a fixed number of input views since aggregation is performed using pooling. In fact, the number of views at runtime can be different from the number of views used during training.

The main advantage of using PSVs is that they eliminate the need to supply rectified images. In other words, the camera parameters are implicitly encoded. However, in order to compute the PSVs, the intrinsic and extrinsic camera parameters need to be either provided in advance or estimated using, for example, Structure-from-Motion techniques as in [36]. Also, these methods require setting in advance the disparity range and its discretisation.

Instead of using PSVs, other methods use the

camera parameters to unproject either the input images [62] or the learned features [37], [38] into either a regular 3D feature grid, by rasterizing the viewing rays with the known camera poses, a 3D frustum of a reference camera [37], or by warping of the features into different parallel frontal planes of the reference camera, each one located at a specific depth. This unprojection aligns the features along epipolar lines, enabling efficient local matching by using either some distance measures such as the Euclidean or cosine distances [38], using a recurrent network [38], or using an encoder composed of multiple convolutional layers producing the probability of each voxel being on the surface of the 3D shape.

Note that the approaches of Kar *et al.* [38] and Ji *et al.* [62] perform volumetric reconstruction and use 3D convolutions. Thus, due to the memory requirements, only a coarse volume of size 32^3 could be estimated. Huang *et al.* [36] overcome this limitation by directly regressing depth from different reference images. Similarly, Yao *et al.* [37] focus on producing the depth map for one reference image at each time. Thus, it can directly reconstruct a large scene.

Table 6 summarizes the performance of these techniques. Note that most of them do not achieve sub-pixel accuracy, require the depth range to be specified in advance and cannot vary it at runtime without re-adjusting the network architecture and retraining it. Also, these methods fail in reconstructing tiny features such as those present in vegetation.

4 DEPTH ESTIMATION BY REGRESSION

Instead of trying to match features across images, methods in this class directly regress disparity/depth from the input images or their learned features [12], [13], [15], [63]. These methods have no direct notion of descriptor matching. They consider a learned, view-based representation for depth reconstruction from either n predefined viewpoints $\{v_1, \dots, v_n\}$, or from any arbitrary viewpoint specified by the user. Their goal is to learn a predictor f (see Section 2), which predicts depth map from an input \mathbf{I} .

4.1 Network architectures

We classify the state-of-the-art into two classes, based on the type of network architectures they use. In the first class of methods, the predictor f is an encoder which directly regresses the depth map [3].

In the second class of methods, the predictor f is composed of an encoder and a top network. The encoder, which learns, using a convolutional network, a function h that maps the input \mathbf{I} into a compact latent representation $\mathbf{x} = h(\mathbf{I}) \in \mathcal{X}$. The space \mathcal{X} is referred to as *the latent space*. The encoder can be designed following any of the architectures discussed in Section 3.1. The top network g takes the compact representation, and eventually the target viewpoint v , and generates

the estimated depth map $\hat{D} = g(h(\mathbf{I}), v) = (g \circ h)(\mathbf{I}, v)$. Some methods use a top network composed of fully connected layers [1], [4], [10], [11]. Others use a decoder composed of upconvolutional layers [2], [13], [44], [63], [64].

The advantage of fully-connected layers is that they aggregate information coming from the entire image, and thus enable the network to infer depth at each pixel using global information. Convolutional operations, on the other hand, can only see local regions. To capture larger spatial relations, one needs to increase the number of convolution layers or use dilated convolutions, *i.e.*, large convolutional filters but with holes

4.1.1 Input encoding networks

In general, the encoder stage is composed of convolutional layers, which capture local interactions between image features, followed by a number of fully-connected layers, which capture global interactions. Some layers are followed by spatial pooling operations to reduce the resolution of the output. For instance, Eigen *et al.* [10], one of the early works that tried to regress depth directly from a single input image, used an encoder composed of five feature extraction layers of convolution and max-pooling followed by one fully-connected layer. This maps the input image of size 304×228 or 576×172 , depending on the dataset, to a latent representation of dimension 1×4096 . Liu *et al.* [4], on the other hand, used 7 convolutional layers to map the input into a low resolution feature map of dimension 512.

Garg *et al.* [3] used this architecture to directly regress depth map from an input RGB images of size 188×620 . The encoder is composed of 7 convolutional layers. The second, third, and fifth layers are followed by pooling layers to reduce the size of the output and thus the number of parameters of the network. The output of the sixth layer is a feature vector, which can be seen as a latent representation of size $16 \times 16 \times 2048$. The last convolutional layer maps this latent representation into a depth map of size 17×17 , which is upsampled using two fully connected layers and three upconvolutional layers, into a depth map of size 176×608 . Since it only relies on convolutional operation to regress depth, the approach does not capture global interactions.

Li *et al.* [1] extended the approach of Eigen *et al.* [10] to operate on superpixels and at multiple scales. Given an image, super-pixels are obtained and multi-scale image patches (at five different sizes) are extracted around the super-pixel centers. All patches of a super-pixel are resized to 227×227 pixels to form a multiscale input to a pre-trained multi-branch deep network (AlexNet or VGGNet). Each branch generates a latent representation of size 1×4096 . The latent representations from the different branches are concatenated together and fed to the top network.

Since the networks process patches, obtaining the entire depth map requires multiple forward passes.

Since its introduction, this approach has been extended in many ways. For instance, Eigen and Fergus [2] showed a substantial improvement by switching from AlexNet (used in [10]) to VGG, which has a higher discriminative power. Also, instead of using fully convolutional layers, Laina *et al.* [64] incorporate residual blocks to ease the training. The encoder is implemented following the same architecture as ResNet50 but without the fully connected layers.

Using repeated spatial pooling reduces the spatial resolution of the feature maps. Although high-resolution maps can be obtained using the refinement techniques of Section 3.1.4, this would require additional computational and memory costs. To overcome this problem, Fu *et al.* [41], removed some pooling layers and replaced some convolutions with dilated convolutions. In fact, convolutional operations are local, and thus, they do not capture the global structure. To enlarge their receptive field, one can increase the size of the filters, or increase the number of convolutional and pooling layers. This, however, would require additional computational and memory costs, and will complicate the network architecture and the training procedure. One way to solve this problem is by using dilated convolutions, *i.e.*, convolutions with filters that have holes [41]. This allows to enlarge the receptive field of the filters without decreasing the spatial resolution or increasing the number of parameters and computation time.

Using this principle, Fu *et al.* [41] proposed an encoding module that operates in two stages. The first stage extracts a dense feature map using an encoder whose last few downsampling operators (pooling, strides) are replaced with dilated convolutions in order to enlarge the receptive field of the filters. The second stage processes the dense feature map using three parallel modules; a full image encoder, a cross channel leaner, and an atrous spatial pyramid pooling (ASPP). The full image encoder maps the dense feature map into a latent representation. It uses an average pooling layer with a small kernel size and stride to reduce the spatial dimension. It is then followed by a fully connected layer to obtain a feature vector, then add a convolutional layer with 1×1 kernel and copy the resultant feature vector into a feature map where each entry has the same feature vector. The ASPP module extracts features from multiple large receptive fields via dilated convolutions, with three different dilation rates. The output of the three modules are concatenated to form the latent representation.

These encoding techniques extract absolute features, ignoring the depth constraints of neighboring pixels, *i.e.*, relative features. To overcome this limitation, Gan *et al.* [65] explicitly model the relationships of different image locations using an affinity layer. They also combine absolute and relative features in

an end-to-end network. In this approach, the input image is first processed by a ResNet50 encoder. The produced absolute feature map is fed into a context network, which captures both neighboring and global context information. It is composed of an affinity layer, which computes correlations between the features of neighboring pixels, followed by a fully-connected layer, which combines absolute and relative features. The output is fed into a depth estimator, which produces a coarse depth map.

4.1.2 Decoding networks

Many techniques first compute a latent representation of the input and then use a top network to decode the latent representation into a coarse depth map. In general, the decoding process can be done with either a series of fully-connected layers [1], [4], [10], [11], or upconvolutional layers [2], [13], [44], [63], [64].

4.1.2.1 Using fully-connected layers: Eigen *et al.* [10], Li *et al.* [1], Eigen and Fergus [2] and Liu *et al.* [4] use a top network composed of two fully-connected layers. The main advantage of using fully connected layers is that their receptive field is global. As such, they aggregate information from the entire image in the process of estimating the depth map. By doing so, however, the number of parameters in the network is high, and subsequently the memory requirement and computation time increase substantially. As such, these methods only estimate low-resolution coarse depth maps, which are then refined using some refinement blocks. For example, Eigen and Fergus [2] use two refinement blocks similar to those used in [10]. The first one produces predictions at a mid-level resolution, while the last one produces high resolution depth maps, at half the resolution of the output. In this approach, the coarse depth prediction network and the first refinement stage are trained jointly, with 3D supervision.

4.1.2.2 Using up-convolutional layers: Dosovitskiy *et al.* [12] extended the approach of Eigen *et al.* [10] by removing the fully-connected layers. Instead, they pass the feature map, *i.e.*, the latent representation (of size $6 \times 8 \times 1024$), directly into a decoder to regress the optical flow in the case of the FlowNetSimple of [12], and a depth map in the case of [2]. In general, the decoder mirrors the encoder. It also includes skip connections, *i.e.*, connections from some layers of the encoder to their corresponding counterpart in the decoder. Dosovitskiy *et al.* [12] use variational refinement to refine the coarse optical flow.

Chen *et al.* [66] used a similar approach to produce dense depth maps given an RGB image with known depth at a few pixels. At training, the approach takes the ground-truth depth map and a binary mask indicating valid ground-truth depth pixels, and generates two other maps: the nearest-neighbor fill of the sparse depth map, and the Euclidean distance transform of

the binary mask. These two maps are then concatenated together and with the input image and used as input to an encoder-decoder, which learns the residual that will be added to the sparse depth map. The network follows the same architecture as in [67]. Note that the same approach has been also used to infer other properties, *e.g.*, the optical flow as in Zhou *et al.* [44].

4.1.3 Combining and stacking multiple networks

Several previous papers showed that stacking and combining multiple networks can lead to significantly improved performance. For example, Ummenhofer and Zhou [15] introduced DeMoN, which takes an image pair as input and predicts the depth map of the left image and the relative pose (egomotion) of the right image with respect to the left. The network consists of a chain of three blocks that iterate over optical flow, depth, and relative camera pose estimation. The first block in the chain, called bootstrap net, is composed of two encoder-decoder networks. It gets the image pair as input and then estimates, using the first encoder-decoder, the optical flow and a confidence map. These, along with the original pair of images, are fed to the second encoder-decoder, which outputs the initial depth and egomotion estimates. The second component, called iterative net, is trained to improve, in a recursive manner, the depth, normal, and motion estimates. Finally, the last component, called refinement net, upsamples, using an encoder-decoder network, the output of the iterative net to obtain high resolution depth maps.

Note that, unlike other techniques such as FlowNetSimple of [12] which require a calibrated pair of images, Ummenhofer and Zhou [15] estimates jointly the relative camera motion and the depth map.

FlowNetSimple of [12] has been later extended by Ilg *et al.* [68] to FlowNet2.0, which achieved results that are competitive with the traditional methods, but with an order of magnitude faster. The idea is to combine multiple FlowNetSimple networks to compute large displacement optical flow. It (1) stacks multiple FlowNetSimple and FlowNetC networks [12]. The flow estimated by each network is used to warp, using a warping operator, the right image onto the left image, and feed the concatenated left image, warped image, estimated flow, and the brightness error, into the next network. This way, the next network in the stack can focus on learning the remaining increment between the left and right images, (2) adds another FlowNetSimple network, called FlowNet-SD, which focuses on small subpixel motion, and (3) uses a learning schedule consisting of multiple datasets. The output of the FlowNet-SD and the stack of multiple FlowNetSimple modules are merged together and processed using a fusion network, which provides the final flow estimation.

Roy *et al.* [69] observed that among all the training data sets currently available, there is limited training data for some depths. As a consequence, deep learning techniques trained with these datasets will naturally achieve low performance in the depth ranges that are under-represented in the training data. Roy *et al.* [69] mitigate the problem by combining CNN with a Neural Regression Forest. A patch around a pixel is processed with an ensemble of binary regression tree, called Convolutional Regression Tree (CRT). At every node of the CRT, the patch is processed with a shallow CNN associated to that node, and then passed to the left or right child node with a Bernouli probability for further convolutional processing. The process is repeated until the patch reaches the leaves of the tree. Depth estimates made by every leaf are weighted with the corresponding path probability. The regression results of every CRT are then fused into a final depth estimation.

Chakrabarti [70] combine global and local methods. The method first maps an input image into a latent representation of size 1×1096 , which is then reshaped into a feature map of size $427 \times 562 \times 64$. In other words, each pixel is represented with a global descriptor (of size 1×64) that characterizes the entire scene. A parallel path takes patches of size 97×97 around each pixel and computes a local feature vector of size 1×1024 . This one is then concatenated with the global descriptor of that pixel and fed into a top network. The whole network is trained to predict, at every image location, depth derivatives of different orders, orientations, and scales. However, instead of a single estimate for each derivative, the network outputs probability distributions that allow it to express confidence about some coefficients, and ambiguity about others. Scene depth is then estimated by harmonizing this overcomplete set of network predictions, using a globalization procedure that finds a single consistent depth map that best matches all the local derivative distributions.

4.1.4 Joint task learning

Depth estimation and many other visual image understanding problems, such as segmentation, semantic labelling, and scene parsing, are strongly correlated and mutually beneficial. Leveraging on the complementarity properties of these tasks, many recent papers proposed to either jointly solve these tasks so that one boosts the performance of another.

To this end, Wang *et al.* [71] follow the CNN structure in [10] but adds additional semantic nodes, in the final layer, to predict the semantic label. Both depth estimation and semantic label prediction are trained jointly using a loss function that is a weighted sum of the depth error and the semantic loss. The overall network is composed of a joint global CNN, which predicts, from the entire image, a coarse depth and

segmentation maps, and a regional CNN, which operates on image segments (obtained by over segmenting the input image) and predicts a more accurate depth and segmentation labels within each segment. These two predictions form unary terms to a hierarchical CRF, which produces the final depth and semantic labels. The CRF includes additional pairwise terms such as pairwise edges between neighboring pixels, and pairwise edges between neighboring segments.

Zhou *et al.* [72] follow the same idea to jointly estimate, from two successive images and in a non-supervised manner, the depth map at each of them, the 6D relative camera pose, and the forward and backward optical flows. The approach uses three separate network, but jointly trained using a cross-task consistency loss: a DepthNet, which estimates depth from two successive frames, PoseNet, which estimates the relative camera pose, and a FlowNet, which estimates the optical flow between the two frames. To handle non-rigid transformations that cannot be explained by the camera motion, the paper exploits the forward-backward consistency check to identify valid regions, *i.e.*, regions that moved in a rigid manner, and avoid enforcing the cross-task consistency in the non-valid regions.

In the approaches of Wang *et al.* [71] and Zhou *et al.* [72], the networks (or network components) that estimate each modality do not directly share knowledge. Collaboration between them is only through a joint loss function. To enable information exchange between the different task, Xu *et al.* [73] proposed an approach that first maps the input image into a latent representation using a CNN. The latent representation is then decoded, using four decoding streams, into a depth map, a normal map, an edge map, and a semantic label map. These multi-modal intermediate information is aggregated using a multi-model distillation module, and then passed into two decoders, one estimates the refined depth map and the other one estimates the refined semantic label map. For the multi-model distillation module, Xu *et al.* [73] investigated three architectures:

- Simple concatenation of the four modalities.
- Concatenating the four modalities and feeding them to two different encoders. One encoder learns the features that are appropriate for inferring depth while the second learns features that are appropriate for inferring semantic labels.
- Using an attention mechanism to guide the message passing between the multi-modal features, before concatenating them and feeding them to the encoder that learns the features for depth estimation or the one which learns the features for semantic labels estimation.

Xu *et al.* [73] showed that the third option obtains remarkably better performance than the others.

Instead of a distillation module, Jiao *et al.* [74] proposed a synergy network whose backbone is

a shared encoder. The network then splits into two branches, one for depth estimation and another for semantic labelling. These two branches share knowledge through lateral sharing units. The network is trained with an attention-driven loss, which guides the network to pay more attention to the distant depth regions during training.

Finally, instead of estimating depth and semantic segmentation in a single iteration, Zhang *et al.* [52] performed it recursively, using Task-Recursive learning. It is composed of an encoder and a decoder network, with a series of residual blocks (ResNet), upsampling blocks, and Task-Attention Modules. The input image is first fed into the encoder and then into the task-recursive decoding to estimate depth and semantic segmentation. In the decoder, the two tasks (depth estimation and segmentation) are alternately processed by adaptively evolving previous experiences of both tasks to benefit each other. A task-attention module is used before each residual block and takes depth and segmentation features from the previous residual block as input. It is composed of a balance unit, to balance the contribution of the features of the two sources. The balanced output is fed into a series of convolutional-deconvolutional layers designed to get different spatial attentions by using receptive field variation. The output is an attention map, which is used to generate the gated depth and segmentation features. These are fused by concatenation followed by one convolutional layer.

While jointly estimating depth and other cues, *e.g.*, semantic labels, significantly improves the performance of both tasks, it requires a large amount of training data annotated with depth and semantic labels.

5 TRAINING

The training process aims to find the network parameters W^* that minimize a loss function \mathcal{L} , *i.e.*, :

$$W^* = \arg \min_W \mathcal{L}(\hat{D}, \Theta, W). \quad (6)$$

Here, Θ is the training data, which can be composed of input images, their associated camera parameters, and/or their corresponding ground-truth depth. We will review in Section 5.1 the different datasets that have been used for training deep learning-based depth reconstruction algorithms, and for evaluating their performances. We will then review the different loss functions (Section 5.2), the degree of supervision required in various methods (Section 5.3), and the domain adaptation and transfer learning techniques (Section 5.3.4).

5.1 Datasets and data augmentation

Unlike traditional 3D reconstruction techniques, training and evaluating deep-learning architectures for

depth reconstruction require large amounts of annotated data. This annotated data should be in the form of natural images and their corresponding depth maps, which is very challenging to obtain. Tables 4 summarizes some of the datasets that have been used in the literature. Some of them have been specifically designed to train, test, and benchmark stereo-based depth reconstruction algorithms. They usually contain pairs of stereo images of real or synthesized scenes, captured with calibrated cameras, and their corresponding disparity/depth information as ground truth. The disparity/depth information can be either in the form of maps at the same or lower resolution as the input images, or in the form of sparse depth values at some locations in the reference image. Some of these datasets contain video sequences and thus are suitable for benchmarking Structure from Motion (SfM) and Simultaneous Localisation and Mapping (SLAM) algorithms.

The datasets that were particularly designed to train and benchmark multiview stereo and single view-based reconstruction algorithms (MVS) are composed of multiple scenes with $n \geq 1$ images per scene. Each image is captured from a different viewpoint.

In general, deep-learning models achieve good results if trained on large datasets. Obtaining the ground-truth depth maps is, however, time-consuming and resource intensive. To overcome this limitation, many papers collect data from some existing datasets and augment them with suitable information and annotations to make them suitable for training and testing deep learning-based depth reconstruction techniques. In general, they use the four following strategies:

- **3D data augmentation.** To introduce more diversity to the training datasets, one can apply to the existing datasets some geometric and photometric transformations, *e.g.*, translation, rotation, and scaling, as well as additive Gaussian noise and changes in brightness, contrast, gamma, and color. Although some transformations are similarity preserving, they still enrich the datasets. One advantage of this approach is that it reduces the network’s generalization error. Also statistical shape analysis techniques [87], [88], [89] can be used to synthesize more 3D shapes from existing ones.
- **Using synthesized 3D models and scenes.** One approach to generate image-depth annotations is by synthetically rendering from 3D CAD models 2D and 2.5D views from various (random) viewpoints, poses, and lighting conditions. They can also be overlaid with random textures.
- **Natural image - 3D shape/scene pairs.** Another approach is to synthesize training data by overlaying images rendered from large 3D model collections on the top of real images such as those in the SUN [90], ShapeNet [91], ModelNet [92],

TABLE 4: Datasets for depth/disparity estimation. “#f” refers to the number of frames per video. “#img./scene” refers to the number of images per scenes. We also refer the reader to [75] for more 3D datasets.

Name	Type	Frame size	Number of (pairs of) images				Video (scene)			Camera params	Disp/Depth
			Total	#train	#val	#test	#f	#train	#test		
CityScapes [76]	real	2048 × 1024	5000	2975	500	1525	—	—	—	—	—
KITTI 2015 [77]	real	1242 × 375	—	—	—	—	400	200	200	4	int+ext sparse
KITTI 2012 [78]	real	1240 × 376	389	194	—	195	—	—	—	—	int+ext sparse
FlyingThings3D [13]	synth.	960 × 540	26066	21818	—	4248	—	2247	—	—	int+ext per-pixel
Monkaa [13]	synth.	960 × 540	8591	8591	—	—	—	8	—	—	int+ext per-pixel
Driving [13]	synth.	960 × 540	4392	4392	—	—	—	1	—	—	int+ext per-pixel
MPI Sintel [79]	synth.	1024 × 436	1041	1041	—	—	35	23	12	50	— per-pixel
SUN3D [80]	rooms	640 × 480	—	2.5M	—	—	—	415	—	—	ext. per-pixel
NYU2 [81]	indoor	640 × 480	—	1449	—	—	—	464	—	—	no per-pixel
RGB-D SLAM [82]	real	640 × 480	—	—	—	—	—	15	4	variable	int+ext per-pixel
MVS-Synth [36]	Urban	1920 × 1080	—	—	—	—	120	—	—	100	int+ext per-pixel
ETH3D [83]	in/outdoor	713 × 438	—	27	—	20	—	5	5	—	int+ext point cloud
DTU [84]	MVS	1200 × 1600	—	—	—	—	80	—	—	49 – 64	int+ext
MVS KITTI2015 [77]	MVS	—	—	—	—	—	200 + 200	—	—	20	—
ETH3D [83]	MVS	6048 × 4032	—	—	—	—	13 + 12	—	—	variable	—
Make3D [85]	Single view	2272 × 1704	534	400	—	134	—	—	—	—	55 × 305
MegaDepth [86]	Single, MVS	—	130K	—	—	—	196	—	—	—	Eucl., ordinal

IKEA [93], and PASCAL 3D+ [94] datasets.

While the last two techniques allow enriching existing training datasets, they suffer from domain bias and thus require using domain adaptation techniques, see Section 5.3.4. Finally, some papers overcome the need for ground-truth depth information by training their deep networks without 3D supervision, see Section 5.3.

5.2 Loss functions

The role of the loss function is to measure at each iteration how far the estimated disparity/depth map \hat{D} is from the real map D , and use it to guide the update of the network weights. In general, the loss function is defined as the sum of two terms:

$$\mathcal{L}(\hat{D}, \Theta, W) = \mathcal{L}_1(\hat{D}, \Theta, W) + \mathcal{L}_2(\hat{D}, \Theta, W). \quad (7)$$

The data term \mathcal{L}_1 measures the error between the ground truth and the estimated depth while the regularization term \mathcal{L}_2 is used to incorporate various constraints, *e.g.*, smoothness. To ensure robustness to spurious outliers, some techniques, *e.g.*, [95], use a truncated loss, which is defined at each pixel x as $\min(\mathcal{L}_x, \psi)$. Here, \mathcal{L}_x denotes the non-truncated loss at pixel x , and ψ is a pre-defined threshold.

There are various loss functions that have been used in the literature. Below, we list the most popular ones. Tables 5, 6, and 7 show how these terms have been used to train depth estimation pipelines.

5.2.1 The data term

The data term of Equation (7) measures the error between the ground truth and the estimated depth. Such error can be quantified using one or a weighted sum of two or more of the error measures described below. The L_2 , the mean absolute difference, the cross-entropy loss, and the Hinge loss require 3D supervision while re-projection based losses can be used

without 3D supervision since they do not depend on ground truth depth/disparity.

(1) The L_2 loss is defined as

$$\mathcal{L}_1^0 = \frac{1}{N} \sum_x \|D(x) - \hat{D}(x)\|^2, \quad (8)$$

where N is the number of pixels being considered.

(2) The mean absolute difference (mAD) between the ground truth and the predicted disparity/depth maps [15], [23], [39], [53] is defined as follows;

$$\mathcal{L}_1^1 = \frac{1}{N} \sum_x \|D(x) - \hat{D}(x)\|_1. \quad (9)$$

Many variants of this loss function have been used. For instance, Tonioni *et al.* [96] avoid explicit 3D supervision by taking d_x as the disparity/depth at pixel x computed using traditional stereo matching techniques, $\hat{D}(x)$ as the estimated disparity, and c_x as the confidence of the estimate at x . They then define a *confidence-guided loss* as:

$$\mathcal{L}_1^2 = \frac{1}{N} \sum_x L(x), \quad L(x) = \begin{cases} c_x |d_x - \hat{d}_x| & \text{if } c_x \geq \epsilon, \\ 0 & \text{otherwise.} \end{cases} \quad (10)$$

Here, ϵ is a user-defined threshold.

Yao *et al.* [37], which first estimate an initial depth map \hat{D}_0 and then the refined one \hat{D} , define the overall loss as the weighted sum of the mean absolute difference between the ground truth D and \hat{D}_0 , and the ground truth D and \hat{D} :

$$\mathcal{L}_1^3 = \frac{1}{N} \sum_x \left\{ \|d(x) - \hat{d}_0(x)\|_1 + \lambda \|d(x) - \hat{d}(x)\|_1 \right\}. \quad (11)$$

Here, $d_x = D(x)$, and λ is a weight factor, which is set to one in [37]. Khamis *et al.* [27], on the other hand, used the two-parameter robust function $\rho(\cdot)$, proposed in [97], to approximate a smoothed L_1 loss.

It is defined as follows:

$$\mathcal{L}_1^4 = \frac{1}{N} \sum_x \rho(d_x - \hat{d}_x, \alpha, c), \text{ where } \alpha = 1, c = 2, \text{ and} \\ \rho(x, \alpha, c) = \frac{|2-\alpha|}{\alpha} \left(\left(\frac{x^2}{c^2|2-\alpha|} + 1 \right)^{\frac{\alpha}{2}} - 1 \right). \quad (12)$$

Other papers, *e.g.*, [28], use the smooth L_1 loss, which is widely used in bounding box regression for object detection because of its robustness and low sensitivity to outliers. It is defined as:

$$\mathcal{L}_1^5 = \frac{1}{N} \sum_x \text{smooth}_{L_1}(d_x - \hat{d}_x), \quad (13)$$

where $\text{smooth}_{L_1}(x) = \begin{cases} 0.5x^2 & \text{if } |x| < 1, \\ |x| - 0.5 & \text{otherwise.} \end{cases}$

Note that some papers restrict the sum to be over valid pixels in order to avoid outliers, or over regions of interests, *e.g.*, foreground or visible pixels [44].

(3) The cross-entropy loss [19], [36]. It is defined as:

$$\mathcal{L}_1^6 = - \sum_x Q(d_x, \hat{d}_x) \log(P(x, \hat{d}_x)). \quad (14)$$

Here, $P(x, \hat{d}_x)$ is the likelihood, as computed by the network, of pixel x having the disparity/depth \hat{d}_x . It is defined in [19], [36] as the 3-pixel error:

$$Q(d_x, \hat{d}_x) = \begin{cases} \lambda_1 & \text{if } d_x = \hat{d}_x \\ \lambda_2 & \text{if } |d_x - \hat{d}_x| = 1 \\ \lambda_3 & \text{if } |d_x - \hat{d}_x| = 2 \\ 0 & \text{otherwise.} \end{cases} \quad (15)$$

Luo *et al.* [19] set $\lambda_1 = 0.5$, $\lambda_2 = 0.2$, and $\lambda_3 = 0.05$.

(4) The sub-pixel cross-entropy loss \mathcal{L}_1^7 . This loss, introduced by Tulyakov *et al.* [60], enables faster convergence and better accuracy at the sub-pixel level. It is defined using a discretized Laplace distribution centered at the ground-truth disparity:

$$Q(d_x, \hat{d}_x) = \frac{1}{Z} e^{-\frac{1}{b}|d_x - \hat{d}_x|}, \quad Z = \sum_d e^{-\frac{1}{b}|d_x - d|}. \quad (16)$$

Here, d_x is the ground-truth disparity at pixel x and \hat{d}_x is the estimated disparity at the same pixel.

(5) The hinge loss criterion [18], [21]. It is computed by considering pairs of examples centered around the same image position where one example belongs to the positive and one to the negative class. Let s_+ be the output of the network for the positive example, s_- be the output of the network for the negative example, and let m , the margin, be a positive real number. The hinge loss for that pair of examples is defined as:

$$\mathcal{L}_1^8 = \max(0, m + s_- - s_+). \quad (17)$$

It is zero when the similarity of the positive example is greater than the similarity of the negative example by at least the margin m , which is set to 0.2 in [18].

(6) The re-projection (inverse warping) loss. Obtaining 3D ground truth data is very expensive. To

overcome this issue, some techniques measure the loss based on the re-projection error. The rationale is that if the estimated disparity/depth map is as close as possible to the ground truth, then the discrepancy between the reference image and any of the other images but unprojected using the estimated depth map onto the reference image, is also minimized. It can be defined in terms of the photometric error [95], [98], also called per-pixel L_1 loss [14], or image reconstruction error [29]. It is defined as the L_1 norm between the reference image I_{ref} and \tilde{I}_t , which is I_t but unwrapped onto I_{ref} using the camera parameters:

$$\mathcal{L}_1^9 = \frac{1}{N} \sum_x \|I_{ref}(x) - \tilde{I}_t(x)\|_1. \quad (18)$$

It can also be defined using the distance between the features \mathbf{f} of the reference image and the features $\tilde{\mathbf{f}}_t$ of any of the other images but unwrapped onto the view of the reference image using the camera parameters and the computed depth map [25]:

$$\mathcal{L}_1^{10} = \frac{1}{N} \sum_x \|\mathbf{f}(x) - \tilde{\mathbf{f}}_t(x)\|_1. \quad (19)$$

Other terms can be added to the re-projection loss. Examples include the L_1 difference between the gradients of I_{ref} and the gradient of \tilde{I}_t [29]:

$$\mathcal{L}_1^{11} = \frac{1}{N} \sum_x \|\nabla I_{ref}(x) - \tilde{\nabla} I_t(x)\|_1, \quad (20)$$

and the structural dissimilarity between patches in I_{ref} and in \tilde{I}_t [29], [99]. We denote this loss by \mathcal{L}_1^{12} .

(7) Matching loss. Some methods, *e.g.*, [18], [20], [21], train the feature matching network separately from the subsequent disparity computation and refinement blocks, using different loss functions. Chen *et al.* [20] use a loss that measures the L_2 distance between the predicted matching score and the ground-truth score:

$$\mathcal{L}_1^{13} = \|\text{predicted_score}(x, d) - \text{label}(x, d)\|, \quad (21)$$

where $\text{label}(x, d) \in \{0, 1\}$ is the ground-truth label indicating whether the pixel $x(i, j)$ on the left image corresponds to the pixel $(i - d, j)$ on the right image, and $\text{predicted_score}(x, d)$ is the predicted matching score for the same pair of pixels.

(8) The semantic loss. Some papers incorporate semantic cues, *e.g.*, segmentation [25] and edge [31] maps, to guide the depth/disparity estimation. These can be either provided at the outset, *e.g.*, estimated with a separate method as in [31], or estimated jointly with the depth/disparity map using the same network trained end-to-end. The latter case requires a semantic loss. For instance, Yang *et al.* [25], which use segmentation as semantics, define the semantic loss \mathcal{L}_1^{13} as the distance between the classified warped maps and ground-truth labels. Song *et al.* [31], which

use edge probability map as semantics, define the semantic loss as follows;

$$\mathcal{L}_1^{14} = \frac{1}{N} \sum_x \left\{ |\partial_u d_x| e^{-|\partial_u \xi_x|} + |\partial_v d_x| e^{-|\partial_v \xi_x|} \right\}, \quad (22)$$

where $x = (u, v)$ and ξ is the edge probability map.

5.2.2 The regularization term

In general, one can make many assumptions about the disparity/depth map and incorporate them into the regularization term of Equation (7). Examples of constraints include: smoothness [29], left-right consistency [29], maximum depth [29], and scale-invariant gradient loss [15]. The regularization term can then be formed using a weighted sum of these losses.

(1) Smoothness. It can be measured using the magnitude of the first or second-order gradient of the estimated disparity/depth map. For instance, Yang *et al.* [25] used the L_1 norm of the first-order gradient:

$$\mathcal{L}_2^1 = \frac{1}{N} \sum_x \{(\nabla_u d_x) + (\nabla_v d_x)\}, x = (u, v). \quad (23)$$

Here ∇ is the gradient operator. Zhou *et al.* [95] and Vijayanarasimhan *et al.* [100] define smoothness as the L_2 norm of the second-order gradient:

$$\mathcal{L}_2^2 = \frac{1}{N} \sum_x \{(\nabla_u^2 d_x)^2 + (\nabla_v^2 d_x)^2\}. \quad (24)$$

Zhong *et al.* [29] used the second-order gradient but weighted with the image's second-order gradients:

$$\mathcal{L}_2^3 = \frac{1}{N} \sum_x \left\{ |\nabla_u^2 d_x| e^{-|\nabla_u^2 I_{left}(x)|} + |\nabla_v^2 d_x| e^{-|\nabla_v^2 I_{left}(x)|} \right\}. \quad (25)$$

Finally, Tonioni *et al.* [96] define the smoothness at a pixel x as the absolute difference between the disparity predicted at x and those predicted at each pixel y within a certain predefined neighborhood \mathcal{N}_x around the pixel x . This is then averaged over all pixels:

$$\mathcal{L}_2^4 = \frac{1}{N} \sum_x \sum_{y \in \mathcal{N}_x} |d_x - d_y|. \quad (26)$$

(2) Consistency. Zhong *et al.* [29] introduced the loop-consistency loss, which is constructed as follows; Consider the left image I_{left} and the synthesized image \tilde{I}_{left} obtained by warping the right image to the left image coordinate with the disparity map defined on the right image. A second synthesized left image $\tilde{\tilde{I}}$ is generated by warping the left image to the right image coordinates by using the disparities at the left and right images, respectively. The loop consistency loss consistency term is then defined as:

$$\mathcal{L}_2^5 = |\tilde{\tilde{I}} - I_{left}|. \quad (27)$$

Godard *et al.* [63] introduced the left-right consistency term, which attempts to make the left-view disparity map be equal to the projected right-view disparity

map. It can be seen as a linear approximation of the loop consistency and is defined as follows;

$$\mathcal{L}_2^6 = \frac{1}{N} \sum_x |d_x - \tilde{d}_x|, \quad (28)$$

where \tilde{d} is the disparity at the right image but reprojected onto the coordinates of the left image.

(3) Maximum-depth heuristic. There may be multiple warping functions that achieve similar warping loss, especially for textureless areas. To provide strong regularization in these areas, Zhong *et al.* [29] use the Maximum-Depth Heuristic (MDH) [101], which is defined as the sum of all depths/disparities:

$$\mathcal{L}_2^7 = \frac{1}{N} \sum_x |d_x|. \quad (29)$$

(4) Scale-invariant gradient loss [15], defined as:

$$\mathcal{L}_2^8 = \sum_{h \in A} \sum_x \|g_h[D](x) - g_h[\hat{D}](x)\|_2, \quad (30)$$

where $A = \{1, 2, 4, 8, 16\}$, $x = (i, j)$, $f_{i,j} \equiv f(i, j)$, and

$$g_h[f](i, j) = \left(\frac{f_{i+h,j} - f_{i,j}}{|f_{i+h,j} - f_{i,j}|}, \frac{f_{i,j+h} - f_{i,j}}{|f_{i,j+h} - f_{i,j}|} \right)^T. \quad (31)$$

5.3 Degree of supervision

Supervised methods for depth estimation, which have achieved promising results, rely on large quantities of ground truth depth data. However, obtaining ground-truth depth data, either manually or using traditional stereo matching algorithms or 3D scanning devices, *e.g.*, Kinect, is extremely difficult and expensive, and is prone to noise and inaccuracies. Several mechanisms have been recently proposed in the literature to make the 3D supervision as light as possible. Below, we discuss the most important ones.

5.3.1 Supervision with stereo images

Godard *et al.* [63] exploit the left-right consistency to perform unsupervised depth estimation from a monocular image. The approach is trained, without 3D supervision, using stereo pairs. At runtime, it only requires one input image and returns the disparity map from the same view as the input image. For this, the approach uses the left-right consistency loss of Equation (28), which attempts to make the left-view disparity map be equal to the projected right-view disparity map.

Tonioni *et al.* [96] fine-tune pre-trained networks without any 3D supervision by using stereo pairs. The idea is leverage on traditional stereo algorithms and state-of-the-art confidence measures in order to fine-tune a deep stereo model based on disparities provided by standard stereo algorithms that are deemed as highly reliable by the confidence measure. This is done by minimizing a loss function made out of

two terms: a confidence-guided loss and a smoothing term.

Note that while stereo-based supervision does not require ground-truth 3D labels, these techniques usually rely on the availability of calibrated stereo pairs during training.

5.3.2 Supervision with camera's aperture

Srinivasan *et al.* [102]'s approach uses as supervision the information provided by a camera's aperture. It introduces two differentiable aperture rendering functions that use the input image and the predicted depths to simulate depth-of-field effects caused by real camera apertures. The depth estimation network is trained end-to-end to predict the scene depths that best explain these finite aperture images as defocused renderings of the input all-in-focus image.

5.3.3 Training with relative/ordinal depth annotation

People, in general, are better at judging relative depth [103], *i.e.*, assessing whether a point A is closer than point B . Chen *et al.* [67] introduced an algorithm for learning to estimate metric depth using only annotations of relative depths. In this approach each image is annotated with only the ordinal relation between a pair of pixels, *i.e.*, point A is closer to point B , further than B , or it is hard to tell. To train the network, a ConvNet in this case, using such ordinal relations, Chen *et al.* [67] introduced an improved ranking loss, which encourages the predicted depth to agree with the ground-truth ordinal relations. It is defined as:

$$\mathcal{L}_1^{15}(\hat{D}, \Theta, W) = \sum_{i=1} N \omega_k \mathcal{L}_k(I, x_k, y_k, l_k, \hat{d}), \quad (32)$$

where ω_k , l_k , and \mathcal{L}_k are, respectively, the weight, the label, and loss of the k -th pair (x_k, y_i) defined as:

$$\mathcal{L}_k = \begin{cases} \log(1 + \exp((- \hat{d}_{xk} + \hat{d}_{yk})l_k)), & \text{if } l_k \neq 0, \\ (\hat{d}_{xk} - \hat{d}_{yk})^2, & \text{otherwise.} \end{cases} \quad (33)$$

Xian *et al.* [104] showed that training with only one pair of ordinal relation for each image is not sufficient to get satisfactory results. They then extended this approach by annotating each image with 3K pairs and showed that they can achieve substantial improvement accuracy. The challenge, however, is how to cheaply get such large number of relative ordinal annotations. They propose to use optical flow maps from web stereo images. Note that at runtime, both methods take a single image of size 384×384 and output a dense depth map of the same size.

5.3.4 Domain adaptation and transfer learning

Supervised deep learning often suffers from the lack of sufficient training data. Also, when using range sensors, noise is often present and the measurements can be very sparse. Kuznetsov *et al.* [105] propose an approach to depth map prediction from monocular

images that learns in a semi-supervised way. The idea is to use sparse ground-truth depth for supervised learning, while enforcing the deep network to produce photoconsistent dense depth maps in a stereo setup using a direct image alignment / reprojection loss.

While obtaining ground-truth depth annotations of real images is challenging and time consuming, synthetic images with their corresponding depth maps can be easily generated using computer graphics techniques. However, the domain of real images is different from the domain of graphics-generated images. Recently, several domain adaptation strategies have been proposed to solve this domain bias issue. These allow training on synthetic data and transfer what has been learned to the domain of real images.

Domain adaptation methods for depth estimation can be classified into two categories. Methods in the first category transform the data of one domain to look similar in style to the data in the other domain. For example, Atapour-Abarghoue *et al.* [106] proposed a two-staged approach. The first stage includes training a depth estimation model using synthetic data. The second stage is trained to transfer the style of synthetic images to real-world images. By doing so, the style of real images is first transformed to match the style of synthetic data and then fed into the depth estimation network, which has been trained on synthetic data. Zheng *et al.* [107] performed the opposite; it transforms the synthetic images to become more realistic and use them to train the depth estimation network. Guo *et al.* [108], on the other hand, trains a stereo matching network using synthetic data to predict occlusion maps and disparity maps of stereo image pairs. In a second step, a monocular depth estimation network is trained on real data by distilling the knowledge of the stereo network [109]. These methods use adversarial learning.

Methods in the second class operate on the network architecture and the loss functions used for their training. Kundu *et al.* [110] introduced AdaDepth, an unsupervised mechanism for domain adaptation. The approach uses an encoder-decoder architecture of the form $\hat{D} = g(h(\mathbf{I}_s))$. It is first trained, in a supervised manner, using synthetic data \mathbf{I}_s . Let g_s and h_s be the decoding and encoding functions learned from synthetic data. Let g_t and h_t be the decoding and encoding functions that correspond to real data \mathbf{I}_t . Kundu *et al.* [110] assume that $g_t = g_s = g$. Its goal is to match the distributions of the latent representations generated by h_s and h_t . This is done by initializing the network with the weights that have been learned using synthetic data. It then uses adversarial learning to minimize an objective function that discriminates between $g_t(\mathbf{I}_t)$ and $g_s(\mathbf{I}_s)$, and another objective function that discriminates between \hat{d}_s and $g(h_t(\mathbf{I}_t))$. The former ensures that real data, when fed to the encoder, are mapped to the same latent space as the

one learned during training. The latter ensures that inferences through the corresponding transformation functions $g(h_s(\cdot))$ and $g(h_t(\cdot))$ are directed towards the same output density function.

6 DISCUSSION AND COMPARISON

This section discusses some state-of-the-art techniques using quantitative and qualitative performance criteria.

6.1 Evaluation metrics and criteria

The most commonly used quantitative metrics for evaluating the performance of a depth estimation algorithm include (the lower these metrics are the better);

- *Computation time* at training and runtime. While one can afford large computation time during training, some applications may require realtime performance at runtime.
- *Memory footprint*. In general deep neural networks have a large number of parameters. Some of them operate on volumes using 3D convolutions. This would require large memory storage, which can affect their performance at runtime.
- *The End-Point Error (EPE)*. Called also geometric error, it is defined as the distance between the ground truth D and the predicted disparity/depth \hat{D} , i.e., $EPE(D, \hat{D}) = \|D - \hat{D}\|$. This metric has two variants: Avg-Noc and Avg-ll. The former is measured in non-occluded areas while the latter is measured over the entire image.
- *Percentage of Erroneous pixels (PE)*. It is defined as the percentage of pixels where the true and predicted disparity/depth differ with more than a predefined threshold ϵ . Similar to the EPE, this error can be measured on non-occluded areas (Out-Noc) and over the entire image (Out-All).
- *The bad pixel error (D1)*. It is defined as the percentage of disparity/depth errors below a threshold. This metric is computed in non-occluded (Noc) and in all pixels (All), in background (bg) and in foreground (fg) pixels.
- *Absolute relative difference*. It is defined as the average over all the image pixels of the L_1 distance between the ground-truth and the estimate depth/disparity, but scaled by the estimated depth/disparity:

$$\text{Abs rel. diff} = \frac{1}{N} \sum \frac{|d_i - \hat{d}_i|}{\hat{d}_i}. \quad (34)$$

- *Squared relative difference*. It is defined as the average over all the image pixels of the L_2 distance between the ground-truth and the estimate depth / disparity, but scaled by the estimated

depth/disparity:

$$\text{Abs rel. diff} = \frac{1}{N} \sum \frac{|d_i - \hat{d}_i|^2}{\hat{d}_i}. \quad (35)$$

- *The linear Root Mean Square Error*. It is defined as follows:

$$\text{RMSE(linear)} = \sqrt{\frac{1}{N} \sum |d_i - \hat{d}_i|^2}. \quad (36)$$

- *The log Root Mean Square Error*. It is defined as follows:

$$\text{RMSE(log)} = \sqrt{\frac{1}{N} \sum |\log d_i - \log \hat{d}_i|^2}. \quad (37)$$

The accuracy is generally evaluated using the following metrics (the higher these metrics are the better);

- *Maximum relative error*. It is defined as the percentage of pixels i such that

$$\max \left(\frac{d_i}{\hat{d}_i}, \frac{\hat{d}_i}{d_i} \right) < \epsilon, \quad (38)$$

where ϵ is a user-defined threshold. It is generally set to 1.25, 1.25², and 1.25³.

- *Density*. It is defined as the percentage of pixels for which depth has been estimated.

In addition to these quantitative metrics, there are several qualitative aspects to consider. Examples include;

- *Degree of 3D supervision*. One important aspect of deep learning-based depth reconstruction methods is the degree of 3D supervision they require during training. In fact, while obtaining multi-view stereo images is easy, obtaining their corresponding ground-truth depth maps and/or pixel-wise correspondences is quite challenging. As such, techniques that require minimal or no 3D supervision are usually preferred over those that require ground-truth depth maps during training.
- *End-to-end training*. In general, the depth estimation pipeline is composed of multiple blocks. In methods, these blocks are trained separately. Others train them jointly in an end-to-end fashion. Some these techniques include a deep learning-based refinement module. Others directly regress the final high resolution map without additional post-processing or regularization.
- *Sub-pixel accuracy*. In general, it is desirable to achieve sub-pixel accuracy without any additional post-processing or regularization.
- *Change in disparity range*. This may require changing the network structure as well as re-training.

We will use these metrics and criteria to compare and discuss existing methods.

6.2 Pairwise stereo matching techniques

Table 5 compares the properties and performance of deep learning-based depth estimation methods from stereo images. Below, we discuss some of them.

TABLE 5: Performance comparison of deep learning-based stereo matching algorithms on the test set of KITTI 2015 benchmark (as of 2019/01/05). PE: percentage of erroneous pixels. EPE: End-Point Error. S1: the bad pixel error. Non-Occ: non-occluded pixels. All: all pixels. fg: foreground pixels. bg: background pixels. Noc: non-occluded pixels only. The bad pixel metric (D1) considers the disparity/depth at a pixel to be correctly estimated if the error is less than 3 pixels or less than 5% of its value.

Method	Description	Training			Avg D1 Non-Occ / Est			Avg D1 All / Est			Avg D1 Non-Occ / All			Avg D1 All / All			Time (s)	Environment
		3D Sup	Loss	End-to-end	D1-fg	D1-bg	D1-all	D1-fg	D1-bg	D1-all	D1-fg	D1-bg	D1-all	D1-fg	D1-bg	D1-all		
MC-CNN Accr [17]	Raw disparity + classic refinement	✓	\mathcal{L}_1^{13}	×	7.64	2.48	3.33	8.88	2.89	3.89	7.64	2.48	3.33	8.88	2.89	3.89	67	Nvidia GTX Titan X (CUDA, Lua / Torch7)
Luo <i>et al.</i> [19]	Raw disparity + classic refinement	✓	\mathcal{L}_1^6	×	7.44	3.32	4.00	8.58	3.73	4.54	7.44	3.32	4.00	8.58	3.73	4.54	1	Nvidia GTX Titan X (Torch)
Chen <i>et al.</i> [20]	Raw disparity + classic refinement	✓	\mathcal{L}_1^{13}	×	—	—	—	—	—	—	—	—	—	—	—	—	—	—
L-ResMatch [21]	Raw disparity + confidence score + classic refinement	✓		o	5.74	2.35	2.91	6.95	2.72	3.42	5.74	2.35	2.91	6.95	2.72	3.42	48	Nvidia Titan-X
Han <i>et al.</i> [22]	Matching network	✓	\mathcal{L}_1^4	×	—	—	—	—	—	—	—	—	—	—	—	—	—	Nvidia GTX Titan Xp
Tulyakov <i>et al.</i> [60]	MC-CNN fast [17] + weakly-supervised learning	—	—	×	9.42	3.06	4.11	10.93	3.78	4.93	9.42	3.06	4.11	10.93	3.78	4.93	1.35	1 core 2.5 Ghz + K40 NVIDIA, Lua-Torch
FlowNetCorr [12]	Refined disparity	✓	\mathcal{L}_1^1	✓	—	—	—	—	—	—	—	—	—	—	—	—	1.12	Nvidia GTX Titan
DispNetCorr [13]	Raw disparity	✓		o	3.72	4.11	4.05	4.41	4.32	4.34	3.72	4.11	4.05	4.41	4.32	4.34	0.06	Nvidia Titan-X
Pang <i>et al.</i> [23]	Raw disparity	✓	\mathcal{L}_1^1	o	3.12	2.32	2.45	3.59	2.48	2.67	3.12	2.32	2.45	3.59	2.48	2.67	0.47	—
Yu <i>et al.</i> [24]	Raw disparity map	✓	\mathcal{L}_1^1	o	—	—	—	—	—	—	5.32	2.06	2.32	5.46	2.17	2.79	1.13	Nvidia 1080Ti
Yang <i>et al.</i> [25] - supp.	Raw disparity	✓	$\mathcal{L}_1^1 + \mathcal{L}_1^{13} + \mathcal{L}_1^2$	✓	3.70	1.76	2.08	4.07	1.88	2.25	3.70	1.76	2.08	4.07	1.88	2.25	0.6	—
Yang <i>et al.</i> [25] - unsup.	Raw disparity	×	$\mathcal{L}_1^9 + \mathcal{L}_1^{13} + \mathcal{L}_1^2$	✓	—	—	—	—	—	—	—	—	7.70	—	—	8.79	0.6	—
Liang <i>et al.</i> [26]	Refined disparity	✓	\mathcal{L}_1^1	✓	—	—	—	—	—	—	2.76	2.07	2.19	3.40	2.25	2.44	0.12	Nvidia Titan-X
Khamis <i>et al.</i> [27]	Raw disparity + hierarchical refinement	✓	\mathcal{L}_1^1 with $\alpha = 1, c = 2$	✓	—	—	—	—	—	—	—	—	—	7.45	4.30	4.83	0.015	Nvidia Titan-X
Gidaris & Komodakis [47]	Refinement only	✓	\mathcal{L}_1^1	o	4.87	2.34	2.76	6.04	2.58	3.16	4.87	2.34	2.76	6.04	2.58	3.16	0.4	Nvidia Titan-X
Chang & Chen [28]	Raw disparity	✓	\mathcal{L}_1^2	o	4.31	1.71	2.14	4.62	1.86	2.32	4.31	1.71	2.14	4.62	1.86	2.32	0.41	Nvidia GTX Titan Xp
Zhong <i>et al.</i> [29]	Raw disparity map	×	$\alpha_1 \mathcal{L}_1^{12} + \alpha_2 \mathcal{L}_1^9 + \alpha_3 \mathcal{L}_1^1 + \alpha_4 \mathcal{L}_2^3 + \alpha_5 \mathcal{L}_2^2 + \alpha_6 \mathcal{L}_2^1$	o	6.13	2.46	3.06	7.12	2.86	3.57	6.13	2.46	3.06	7.12	2.86	3.57	0.8	P100
Kendall <i>et al.</i> [39]	Refined disparity map without refinement module	✓	\mathcal{L}_1^1	✓	5.58	2.02	2.61	6.16	2.21	2.87	5.58	2.02	2.61	6.16	2.21	2.87	0.9	Nvidia GTX Titan X
Standard SGM-Net [30]	Refinement with CNN-based SGM	✓	Weighted sum of path cost and neighbor cost	o	—	—	—	—	—	—	7.44	2.23	3.09	—	—	—	67	Nvidia Titan-X
Signed SGM-Net [30]	Refinement with CNN-based SGM	✓	Weighted sum of path cost and neighbor cost	o	7.43	2.23	3.09	8.64	2.66	3.66	7.43	2.23	3.09	8.64	2.66	3.66	67	Nvidia Titan-X
Cheng <i>et al.</i> [53]	Refinement	✓	\mathcal{L}_1^1	o	2.67	1.40	1.61	2.88	1.51	1.74	2.67	1.40	1.61	2.88	1.51	1.74	0.5	GPU @ 2.5 Ghz (C/C++)
EdgeStereo [31]	Raw disparity	✓	$\sum_{s=1}^{s_{\max}} (\mathcal{L}_1^1 + \alpha \mathcal{L}_1^{14})_{sc}$	×	3.04	1.70	1.92	3.39	1.85	2.10	3.04	1.70	1.92	3.39	1.85	2.10	0.32	Nvidia GTX Titan Xp
Tulyakov <i>et al.</i> [32]	Disparity with sub-pixel accuracy	✓	\mathcal{L}_1^1	o	3.63	2.09	2.36	4.05	2.25	2.58	3.63	2.09	2.36	4.05	2.25	2.58	0.5	1 core @ 2.5 Ghz (Python)
Jie <i>et al.</i> [33]	Refined disparity with DL	✓	\mathcal{L}_1^1	✓	4.19	2.23	2.55	5.42	2.55	3.03	4.19	2.23	2.55	5.42	2.55	3.03	49.2	Nvidia GTX Titan X
Seki <i>et al.</i> [59]	Raw disparity, confidence map, SGM-based refinement	✓	\mathcal{L}_1^2	o	7.71	2.27	3.17	8.74	2.58	3.61	7.71	2.27	3.17	8.74	2.58	3.61	68	Nvidia GTX Titan X
Kuzmin <i>et al.</i> [111]	Only aggregated cost volume	✓	\mathcal{L}_1^2	o	10.11	4.81	5.68	11.35	5.32	6.32	10.11	4.82	5.69	11.35	5.34	6.34	0.03	GPU @ 2.5 Ghz (C/C++)
Tonioni <i>et al.</i> [96]	Unsupervised adaptation - DispNetCorrID [13] + CENSUS [112]	✓	$\mathcal{L}_1^1 + \alpha \mathcal{L}_2^4$	NA	—	—	—	—	—	—	—	—	—	—	—	0.76	—	GPU @ 2.5 Ghz (Python)

6.2.1 Degree of supervision

Most of the state-of-the-art methods require ground-truth depth maps to train their deep learning models. This is reflected in the loss functions they use to train the networks. For instance, Flynn *et al.* [14], Kendall *et al.* [39], Pang *et al.* [23], Cheng *et al.* [53], and Liang *et al.* [26] minimize the L_1 distance between the estimated disparity/depth and the ground truth (Equation (9)), while Luo *et al.* [19] minimize the cross-entropy loss of Equation (14). Khamis *et al.* [27] used the same approach but by using the two-parameter robust function (Equation (12)). Chen *et al.* [20], which formulated the stereo matching problem as a classification problem, trained their network to classify whether pixel x on the left image and pixel $x - d$ on the right image are in correspondence (positive class) or not (negative class). The loss is then defined as the L_2 distance between the output of the network for the pixel pair $(x, x - d)$ and the ground-truth label (0 or 1) of this pair of pixels.

In general, obtaining ground-truth disparity/depth

maps is very challenging. As such, techniques that do not require 3D supervision are more attractive. The key to training without 3D supervision is the use of loss functions that are based on the reprojection error, *e.g.*, Equation (18). This approach has been adopted in recent techniques, *e.g.*, Zhou *et al.* [95] and Yang *et al.* [25]. One limitation of these techniques is that they assume that the camera parameters are known so that the unwarping or re-projection onto the coordinates of the other image can be calculated. Some techniques, *e.g.*, [15], assume that the camera parameters are unknown and regress them at the same time as depth/disparity in the same spirit as Structure from Motion (SfM) or visual SLAM.

As shown in Table 5, methods that are trained with 3D supervision achieve a better performance at runtime than those without 3D supervision. For example, Yang *et al.* [25] evaluated their networks in both modes and showed that the supervised one achieved and average D1-all (All/All) of 2.25% compared to 8.79% for the unsupervised one.

6.2.2 Accuracy and disparity range

Based on the metrics of Section 6, the unsupervised adaptation method of Tonioni *et al.* [96] boosted significantly the performance of DispNetCorr1D [13] (from 4.34 on Avg D1 All/All (D1-all) to 0.76). This suggests that such adaptation module can be used to boost the performance of the other methods.

Note that only a few methods could achieve sub-pixel accuracy. Examples include the approach of Tulyakov *et al.* [32], which uses the sub-pixel MAP approximation instead of the softargmin. Also, Tulyakov *et al.* [32]’s approach allows changing the disparity range at runtime without retraining the network.

6.2.3 Computation time and memory footprint

Computation time and memory footprint, which in general are interrelated, are very important especially at runtime. Based on Table 5, we can distinguish three types of methods; Slow methods, average-speed methods, which produce a depth map in around one seconds, and fast methods, which require less than 0.1 seconds to estimate a single depth map.

Slow methods require more than 40 seconds to estimate one single depth map. There are multiple design aspects that make these method slow. For instance, some of them perform multiple forward passes as in [30]. Others either deepen the network by using a large number of layers including many fully connected layers, especially in the similarity computation block as in the MC-CNN Acc of [17] and the L-ResMatch of [21]), or use multiple subnetworks. Other methods estimate the depth map in a recurrent fashion, *e.g.*, by using multiple convLSTM blocks as in Jie *et al.* [33].

According to Table 5, the approach of Khamis *et al.* [27] is the fastest one as it produces, at run time, a disparity map in 15ms, with a subpixel accuracy of 0.03, which corresponds to an error of less than 3cm at 3m distance from the camera. In fact, Khamis *et al.* [27] observed that most of the time and compute is spent matching features at higher resolutions, while most of the performance gain comes from matching at lower resolutions. Thus, they compute the cost volume by matching features at low resolution. An efficient refinement module is then used to upsample the low resolution depth map to the input resolution.

Finally, t Mayer *et al.* [13] and Kendall *et al.* [39] can run very fast, with 0.06s and 0.9s consumed on a single Nvidia GTX Titan X GPU, respectively. However, disparity refinement is not included in these networks, which limits their performance.

6.3 Multiview stereo techniques

Table 6 compares the properties and performance of five deep learning-based multiview stereo reconstruction algorithms. Note that the related papers have reported performance results using different datasets.

6.3.1 Degree of supervision

Most of the methods described in Table 6 are trained using 3D supervision. The only exception is the approach of Flynn *et al.* [14], which is trained using a posed set of images, *i.e.*, images with known camera parameters. At training, the approach takes a set of images, leaves one image out, and learns how to predict it from the remaining ones. The rational is that providing a set of posed images is much simpler than providing depth values at each pixel in every reference image.

6.3.2 Accuracy and depth range

In terms of accuracy, the approach of Huang *et al.* [36] seems to outperform the state-of-the art, see Table 6. However, since these methods have been evaluated on different datasets, it is not clear whether they would achieve the same level of accuracy on other datasets. As such, the accuracy results reported in Table 6 are just indicative not conclusive.

Finally, since most of the MVS methods rely on Plane Sweep Volumes or image/feature umprojection onto depth planes, the depth range needs to be set in advance. Changing the depth range and its discretization at runtime would require re-training the methods.

6.4 Depth regression techniques

Table 7 summarizes the properties and compares the performance of some of the state-of-the-art methods for deep learning-based depth regression on KITTI2012, Make3D, and NYUDv2 datasets.

As shown in this table, the methods of Jiao *et al.* [74] and Fu *et al.* [41] seem to achieve the best accuracy on NYUDv2 dataset. Their common property is the way they handle different depth ranges. In fact, previous methods treat near and far depth values equally. As such, most of them achieve good accuracy in near depth values but their accuracy drops for distant depth values. Jiao *et al.* [74] proposed a new loss function that pays more attention to distant depths. Fu *et al.* [41], on the other hand, formulated depth estimation as a classification problem. The depth range is first discretized into intervals. The network then learn to classify each image pixel into one of the depth intervals. However, instead of using uniform discretization, Fu *et al.* [41] used a spacing increasing discretization.

Another observation from Table ?? is that recent techniques trained without 3D supervision, *e.g.*, by using stereo images and re-projection loss, are becoming very competitive since their performances are close to techniques that use 3D supervision. Kuznietsov *et al.* [105] showed that the performance can be even further improved using semi-supervised techniques where the network is first trained with 3D supervision and then fine-tuned with stereo supervision. Also,

images, and cannot vary the number of input images at training and testing without re-training. The former is mainly due to the computation and memory requirements of most of the deep learning techniques. Developments in high performance computing can address this issue in the future. However, developing lighter deep architectures remains desirable especially if to be deployed in mobile and portable platforms.

- *Accuracy*: Although refinement modules can improve the resolution of the estimated depth maps, it is still small compared to the resolution of the images that can be recovered. As such, deep learning techniques find it difficult to recover small details, *e.g.*, vegetation and hair. Also, most of the techniques discretize the depth range. Although some methods can achieve sub-pixel accuracy, changing the depth range, and the discretization frequency, requires retraining the networks. Another issue is the accuracy, which, in general, varies for different depth ranges. Some of the recent works, *e.g.*, [74], tried to address this problem, but it still remains an open and challenging problem since it is highly related to the data bias issue and the type of loss functions used to train the network. Accuracy of existing methods is also affected by complex scenarios, *e.g.*, occlusions and highly cluttered scenes, and objects with complex material properties.
- *Performance*: Complex deep networks are very expensive in terms of memory requirements. Memory footprint is even a major issue when dealing with high resolution images and when aiming to reconstruct high resolution depth maps. While this can be mitigated by using multi-scale and part-based reconstruction techniques, it can result in high computation time.
- *Training*: Deep learning techniques rely heavily on the availability of training datasets annotated with ground-truth labels. Obtaining ground-truth labels for depth reconstruction is very expensive. Existing techniques mitigate this problem by either designing loss functions that do not require 3D annotations, or use domain adaptation and transfer learning strategies. The former, however, requires calibrated cameras. Domain adaptation techniques are recently attracting more attention since, with these techniques, one can train with synthetic data, which are easy to obtain, and real-world data.
- *Data bias and generalization*: Most of the recent deep learning-based depth reconstruction techniques have been trained and tested on publicly available benchmarks. While this gives an indication on their performances, it is not clear yet how do they generalize and perform on completely unseen images, from a completely different category. Thus, we expect in the future

to see the emergence of large datasets, similar to ImageNet but for 3D reconstruction. Developing self-adaptation techniques, *i.e.*, techniques that can adapt themselves to new scenarios in real time or with minimum supervision, is one promising direction for future research.

8 CONCLUSION

This paper provided a comprehensive survey of the recent developments in depth reconstruction using deep learning techniques. Despite its infancy, these techniques are achieving acceptable results, and some recent developments are even competing, in terms of accuracy of the results, with traditional techniques. We have seen that, since 2014, more than 100 papers on the topic have been published in major computer vision and machine learning conferences and journals, and more new papers are being published even during the final stage of this submission. We believe that since 2014, we entered a new era where data-driven and machine learning techniques play a central role in image-based depth reconstruction.

Finally, there are several related topics that have not been covered in this survey. Examples include:

- Synthesis of novel 2D views from one or multiple images, which use similar formulations as depth estimation, see for example [5], [6], [7], [8], [9].
- Structure-from-Motion (SfM) and Simultaneous Localization and Mapping (SLAM), which aim to recover at the same time depth maps and (relative) camera pose (or camera motion). Interested readers can refer to recent papers such as [13], [100], [116].
- Image-based object reconstruction algorithms, which aim to recover the entire 3D geometry of objects from one or multiple images.

While these topics are strongly related to depth estimation, they require a separate survey given the large amount of work that has been dedicated to them in the past 4 to 5 years.

REFERENCES

- [1] B. Li, C. Shen, Y. Dai, A. Van Den Hengel, and M. He, "Depth and surface normal estimation from monocular images using regression on deep features and hierarchical CRFs," in *IEEE CVPR*, 2015, pp. 1119–1127.
- [2] D. Eigen and R. Fergus, "Predicting depth, surface normals and semantic labels with a common multi-scale convolutional architecture," in *IEEE ICCV*, 2015, pp. 2650–2658.
- [3] R. Garg, V. K. BG, G. Carneiro, and I. Reid, "Unsupervised CNN for single view depth estimation: Geometry to the rescue," in *ECCV*. Springer, 2016, pp. 740–756.
- [4] F. Liu, C. Shen, G. Lin, and I. D. Reid, "Learning depth from single monocular images using deep convolutional neural fields," *IEEE PAMI*, vol. 38, no. 10, pp. 2024–2039, 2016.
- [5] J. Yang, S. E. Reed, M.-H. Yang, and H. Lee, "Weakly-supervised disentangling with recurrent transformations for 3D view synthesis," in *NIPS*, 2015, pp. 1099–1107.
- [6] T. D. Kulkarni, W. F. Whitney, P. Kohli, and J. Tenenbaum, "Deep convolutional inverse graphics network," in *Advances in Neural Information Processing Systems*, 2015, pp. 2539–2547.

- [7] M. Tatarchenko, A. Dosovitskiy, and T. Brox, "Multi-view 3D models from single images with a convolutional network," in *ECCV*. Springer, 2016, pp. 322–337.
- [8] T. Zhou, S. Tulsiani, W. Sun, J. Malik, and A. A. Efros, "View synthesis by appearance flow," in *ECCV*. Springer, 2016, pp. 286–301.
- [9] E. Park, J. Yang, E. Yumer, D. Ceylan, and A. C. Berg, "Transformation-grounded image generation network for novel 3D view synthesis," in *IEEE CVPR*. IEEE, 2017, pp. 702–711.
- [10] D. Eigen, C. Puhrsch, and R. Fergus, "Depth map prediction from a single image using a multi-scale deep network," in *Advances in neural information processing systems*, 2014, pp. 2366–2374.
- [11] X. Wang, D. Fouhey, and A. Gupta, "Designing deep networks for surface normal estimation," in *IEEE CVPR*, 2015, pp. 539–547.
- [12] A. Dosovitskiy, P. Fischer, E. Ilg, P. Hausser, C. Hazirbas, V. Golkov, P. Van Der Smagt, D. Cremers, and T. Brox, "FlowNet: Learning optical flow with convolutional networks," in *IEEE ICCV*, 2015, pp. 2758–2766.
- [13] N. Mayer, E. Ilg, P. Hausser, P. Fischer, D. Cremers, A. Dosovitskiy, and T. Brox, "A large dataset to train convolutional networks for disparity, optical flow, and scene flow estimation," in *IEEE CVPR*, 2016, pp. 4040–4048.
- [14] J. Flynn, I. Neulander, J. Philbin, and N. Snavely, "DeepStereo: Learning to predict new views from the world's imagery," in *IEEE CVPR*, 2016, pp. 5515–5524.
- [15] B. Ummenhofer, H. Zhou, J. Uhrig, N. Mayer, E. Ilg, A. Dosovitskiy, and T. Brox, "Demon: Depth and motion network for learning monocular stereo," in *IEEE CVPR*, vol. 5, 2017, p. 6.
- [16] D. Scharstein and R. Szeliski, "A taxonomy and evaluation of dense two-frame stereo correspondence algorithms," *IJCV*, vol. 47, no. 1-3, pp. 7–42, 2002.
- [17] J. Zbontar and Y. LeCun, "Computing the stereo matching cost with a convolutional neural network," in *IEEE CVPR*, 2015, pp. 1592–1599.
- [18] —, "Stereo matching by training a convolutional neural network to compare image patches," *Journal of Machine Learning Research*, vol. 17, no. 1-32, p. 2, 2016.
- [19] W. Luo, A. G. Schwing, and R. Urtasun, "Efficient deep learning for stereo matching," in *IEEE CVPR*, 2016, pp. 5695–5703.
- [20] w. Chen, X. Sun, L. Wang, Y. Yu, and C. Huang, "A deep visual correspondence embedding model for stereo matching costs," in *IEEE ICCV*, 2015, pp. 972–980.
- [21] A. Shaked and L. Wolf, "Improved stereo matching with constant highway networks and reflective confidence learning," in *IEEE CVPR*, 2017, pp. 4641–4650.
- [22] X. Han, T. Leung, Y. Jia, R. Sukthankar, and A. C. Berg, "MatchNet: Unifying feature and metric learning for patch-based matching," in *IEEE CVPR*, 2015, pp. 3279–3286.
- [23] J. Pang, W. Sun, J. S. Ren, C. Yang, and Q. Yan, "Cascade residual learning: A two-stage convolutional neural network for stereo matching," in *ICCV Workshops*, vol. 7, no. 8, 2017.
- [24] L. Yu, Y. Wang, Y. Wu, and Y. Jia, "Deep stereo matching with explicit cost aggregation sub-architecture," *AAAI*, 2018.
- [25] G. Yang, H. Zhao, J. Shi, Z. Deng, and J. Jia, "SegStereo: Exploiting Semantic Information for Disparity Estimation," *arXiv preprint arXiv:1807.11699*, 2018.
- [26] Z. Liang, Y. Feng, Y. G. H. L. W. Chen, and L. Q. L. Z. J. Zhang, "Learning for disparity estimation through feature constancy," in *IEEE CVPR*, 2018, pp. 2811–2820.
- [27] S. Khamis, S. Fanello, C. Rhemann, A. Kowdle, J. Valentin, and S. Izadi, "Stereonet: Guided hierarchical refinement for real-time edge-aware depth prediction," *ECCV*, 2018.
- [28] J. Chang and Y. Chen, "Pyramid Stereo Matching Network," *CVPR*, 2018.
- [29] Y. Zhong, Y. Dai, and H. Li, "Self-supervised learning for stereo matching with self-improving ability," *arXiv preprint arXiv:1709.00930*, 2017.
- [30] A. Seki and M. Pollefeys, "SGM-Nets: Semi-global matching with neural networks," in *IEEE CVPR Workshops*, 2017, pp. 21–26.
- [31] X. Song, X. Zhao, H. Hu, and L. Fang, "EdgeStereo: A Context Integrated Residual Pyramid Network for Stereo Matching," *ACCV*, 2018.
- [32] S. Tulyakov, A. Ivanov, and F. Fleuret, "Practical Deep Stereo (PDS): Toward applications-friendly deep stereo matching," *NIPS*, 2018.
- [33] Z. Jie, P. Wang, Y. Ling, B. Zhao, Y. Wei, J. Feng, and W. Liu, "Left-right comparative recurrent model for stereo matching," in *IEEE CVPR*, 2018, pp. 3838–3846.
- [34] S. Zagoruyko and N. Komodakis, "Learning to compare image patches via convolutional neural networks," in *IEEE CVPR*, 2015, pp. 4353–4361.
- [35] W. Hartmann, S. Galliani, M. Havlena, L. Van Gool, and K. Schindler, "Learned multi-patch similarity," in *IEEE ICCV*. IEEE, 2017, pp. 1595–1603.
- [36] P.-H. Huang, K. Matzen, J. Kopf, N. Ahuja, and J.-B. Huang, "DeepMVS: Learning Multi-view Stereopsis," in *IEEE CVPR*, 2018, pp. 2821–2830.
- [37] Y. Yao, Z. Luo, S. Li, T. Fang, and L. Quan, "MVSNet: Depth Inference for Unstructured Multi-view Stereo," *ECCV*, 2018.
- [38] A. Kar, C. Häne, and J. Malik, "Learning a multi-view stereo machine," in *NIPS*, 2017, pp. 364–375.
- [39] A. Kendall, H. Martirosyan, S. Dasgupta, P. Henry, R. Kennedy, A. Bachrach, and A. Bry, "End-to-end learning of geometry and context for deep stereo regression," *CoRR*, vol. abs/1703.04309, 2017.
- [40] E. Simo-Serra, E. Trulls, L. Ferraz, I. Kokkinos, P. Fua, and F. Moreno-Noguer, "Discriminative learning of deep convolutional feature point descriptors," in *IEEE ICCV*, 2015, pp. 118–126.
- [41] H. Fu, M. Gong, C. Wang, K. Batmanghelich, and D. Tao, "Deep ordinal regression network for monocular depth estimation," in *IEEE CVPR*, June 2018.
- [42] K. He, X. Zhang, S. Ren, and J. Sun, "Deep residual learning for image recognition," in *IEEE CVPR*, 2016, pp. 770–778.
- [43] H. Park and K. M. Lee, "Look wider to match image patches with convolutional neural networks," *IEEE Signal Processing Letters*, vol. 24, no. 12, pp. 1788–1792, 2017.
- [44] T. Zhou, P. Krahenbuhl, M. Aubry, Q. Huang, and A. A. Efros, "Learning dense correspondence via 3D-guided cycle consistency," in *IEEE CVPR*, 2016, pp. 117–126.
- [45] H. Hirschmuller, "Stereo processing by semiglobal matching and mutual information," *IEEE PAMI*, vol. 30, no. 2, pp. 328–341, 2008.
- [46] J.-H. Lee, M. Heo, K.-R. Kim, and C.-S. Kim, "Single-image depth estimation based on fourier domain analysis," in *IEEE CVPR*, June 2018.
- [47] S. Gidaris and N. Komodakis, "Detect, replace, refine: Deep structured prediction for pixel wise labeling," in *Proc. of the IEEE Conference on Computer Vision and Pattern Recognition*, 2017, pp. 5248–5257.
- [48] X. Qi, R. Liao, Z. Liu, R. Urtasun, and J. Jia, "GeoNet: Geometric Neural Network for Joint Depth and Surface Normal Estimation," in *IEEE CVPR*, June 2018.
- [49] Y. Zhang, S. Khamis, C. Rhemann, J. Valentin, A. Kowdle, V. Tankovich, M. Schoenberg, S. Izadi, T. Funkhouser, and S. Fanello, "ActiveStereoNet: end-to-end self-supervised learning for active stereo systems," *ECCV*, 2018.
- [50] S. Liu, S. De Mello, J. Gu, G. Zhong, M.-H. Yang, and J. Kautz, "Learning affinity via spatial propagation networks," in *NIPS*, 2017, pp. 1520–1530.
- [51] J. Jeon and S. Lee, "Reconstruction-based pairwise depth dataset for depth image enhancement using cnn," in *ECCV*, September 2018.
- [52] Z. Zhang, Z. Cui, C. Xu, Z. Jie, X. Li, and J. Yang, "Joint task-recursive learning for semantic segmentation and depth estimation," in *ECCV*, September 2018.
- [53] X. Cheng, P. Wang, and R. Yang, "Depth estimation via affinity learned with convolutional spatial propagation network," in *ECCV*, September 2018.
- [54] T. Brox and J. Malik, "Large displacement optical flow: descriptor matching in variational motion estimation," *IEEE PAMI*, vol. 33, no. 3, pp. 500–513, 2011.
- [55] P. Krähenbühl and V. Koltun, "Efficient inference in fully connected crfs with gaussian edge potentials," in *NIPS*, 2011, pp. 109–117.
- [56] X. Sun, X. Mei, S. Jiao, M. Zhou, Z. Liu, and H. Wang, "Real-time local stereo via edge-aware disparity propagation," *Pattern Recognition Letters*, vol. 49, pp. 201–206, 2014.

- [57] A. Odena, V. Dumoulin, and C. Olah, "Deconvolution and checkerboard artifacts," *Distill*, vol. 1, no. 10, p. e3, 2016.
- [58] Z. Zhang, C. Xu, J. Yang, Y. Tai, and L. Chen, "Deep hierarchical guidance and regularization learning for end-to-end depth estimation," *Pattern Recognition*, vol. 83, pp. 430–442, 2018.
- [59] A. Seki and M. Pollefeys, "Patch based confidence prediction for dense disparity map," in *BMVC*, vol. 2, no. 3, 2016, p. 4.
- [60] S. Tulyakov, A. Ivanov, and F. Fleuret, "Weakly supervised learning of deep metrics for stereo reconstruction," in *IEEE ICCV*, no. EPFL-CONF-233588, 2017.
- [61] P. Knöbelreiter, C. Reinbacher, A. Shekhovtsov, and T. Pock, "End-to-end training of hybrid cnn-crf models for stereo," in *IEEE CVPR*. IEEE, 2017, pp. 1456–1465.
- [62] M. Ji, J. Gall, H. Zheng, Y. Liu, and L. Fang, "SurfaceNet: an end-to-end 3D neural network for multiview stereopsis," *IEEE ICCV*, 2017.
- [63] C. Godard, O. Mac Aodha, and G. J. Brostow, "Unsupervised monocular depth estimation with left-right consistency," in *CVPR*, vol. 2, no. 6, 2017, p. 7.
- [64] I. Laina, C. Rupprecht, V. Belagiannis, F. Tombari, and N. Navab, "Deeper depth prediction with fully convolutional residual networks," in *3D Vision (3DV)*. IEEE, 2016, pp. 239–248.
- [65] Y. Gan, X. Xu, W. Sun, and L. Lin, "Monocular depth estimation with affinity, vertical pooling, and label enhancement," in *ECCV*, September 2018.
- [66] Z. Chen, V. Badrinarayanan, G. Drozdov, and A. Rabinovich, "Estimating depth from rgb and sparse sensing," in *ECCV*, September 2018.
- [67] W. Chen, Z. Fu, D. Yang, and J. Deng, "Single-image depth perception in the wild," in *Advances in Neural Information Processing Systems*, 2016, pp. 730–738.
- [68] E. Ilg, N. Mayer, T. Saikia, M. Keuper, A. Dosovitskiy, and T. Brox, "Flownet 2.0: Evolution of optical flow estimation with deep networks," in *IEEE CVPR*, vol. 2, 2017, p. 6.
- [69] A. Roy and S. Todorovic, "Monocular depth estimation using neural regression forest," in *IEEE CVPR*, 2016, pp. 5506–5514.
- [70] A. Chakrabarti, J. Shao, and G. Shakhnarovich, "Depth from a single image by harmonizing overcomplete local network predictions," in *Advances in Neural Information Processing Systems*, 2016, pp. 2658–2666.
- [71] P. Wang, X. Shen, Z. Lin, S. Cohen, B. Price, and A. L. Yuille, "Towards unified depth and semantic prediction from a single image," in *IEEE CVPR*, 2015, pp. 2800–2809.
- [72] Y. Zou, Z. Luo, and J.-B. Huang, "DF-Net: Unsupervised Joint Learning of Depth and Flow using Cross-Task Consistency," in *ECCV*, September 2018.
- [73] D. Xu, W. Wang, H. Tang, H. Liu, N. Sebe, and E. Ricci, "Structured attention guided convolutional neural fields for monocular depth estimation," in *The IEEE Conference on Computer Vision and Pattern Recognition (CVPR)*, June 2018.
- [74] J. Jiao, Y. Cao, Y. Song, and R. Lau, "Look deeper into depth: Monocular depth estimation with semantic booster and attention-driven loss," in *ECCV*, September 2018.
- [75] H. Laga, Y. Guo, H. Tabia, R. B. Fisher, and M. Bennamoun, *3D Shape Analysis: Fundamentals, Theory, and Applications*. John Wiley & Sons, 2018.
- [76] M. Cordts, M. Omran, S. Ramos, T. Rehfeld, M. Enzweiler, R. Benenson, U. Franke, S. Roth, and B. Schiele, "The cityscapes dataset for semantic urban scene understanding," in *IEEE CVPR*, 2016, pp. 3213–3223.
- [77] M. Menze and A. Geiger, "Object scene flow for autonomous vehicles," in *IEEE CVPR*, 2015, pp. 3061–3070.
- [78] A. Geiger, P. Lenz, and R. Urtasun, "Are we ready for autonomous driving? the kitti vision benchmark suite," in *IEEE CVPR*. IEEE, 2012, pp. 3354–3361.
- [79] D. J. Butler, J. Wulff, G. B. Stanley, and M. J. Black, "A naturalistic open source movie for optical flow evaluation," in *ECCV*. Springer, 2012, pp. 611–625.
- [80] J. Xiao, A. Owens, and A. Torralba, "Sun3d: A database of big spaces reconstructed using sfm and object labels," in *IEEE ICCV*, 2013, pp. 1625–1632.
- [81] N. Silberman, D. Hoiem, P. Kohli, and R. Fergus, "Indoor segmentation and support inference from rgb-d images," *ECCV*, pp. 746–760, 2012.
- [82] J. Sturm, N. Engelhard, F. Endres, W. Burgard, and D. Cremers, "A benchmark for the evaluation of rgb-d slam systems," in *IEEE/RSJ IROS*, 2012, pp. 573–580.
- [83] T. Schöps, J. L. Schönberger, S. Galliani, T. Sattler, K. Schindler, M. Pollefeys, and A. Geiger, "A multi-view stereo benchmark with high-resolution images and multi-camera videos," in *IEEE CVPR*, vol. 2017, 2017.
- [84] H. Aanaes, R. R. Jensen, G. Vogiatzis, E. Tola, and A. B. Dahl, "Large-scale data for multiple-view stereopsis," *IJCV*, vol. 120, no. 2, pp. 153–168, 2016.
- [85] A. Saxena, M. Sun, and A. Y. Ng, "Make3d: Learning 3d scene structure from a single still image," *IEEE PAMI*, vol. 31, no. 5, pp. 824–840, 2009.
- [86] Z. Li and N. Snavely, "Megadepth: Learning single-view depth prediction from internet photos," in *IEEE CVPR*, June 2018.
- [87] H. Laga, Q. Xie, I. H. Jermyn, A. Srivastava *et al.*, "Numerical inversion of snrf maps for elastic shape analysis of genus-zero surfaces," *IEEE transactions on pattern analysis and machine intelligence*, vol. 39, no. 12, pp. 2451–2464, 2017.
- [88] I. H. Jermyn, S. Kurtek, H. Laga, and A. Srivastava, "Elastic shape analysis of three-dimensional objects," *Synthesis Lectures on Computer Vision*, vol. 12, no. 1, pp. 1–185, 2017.
- [89] G. Wang, H. Laga, N. Xie, J. Jia, and H. Tabia, "The shape space of 3d botanical tree models," *ACM Transactions on Graphics (TOG)*, vol. 37, no. 1, p. 7, 2018.
- [90] J. Xiao, J. Hays, K. A. Ehinger, A. Oliva, and A. Torralba, "Sun database: Large-scale scene recognition from abbey to zoo," in *IEEE CVPR*. IEEE, 2010, pp. 3485–3492.
- [91] A. X. Chang, T. Funkhouser, L. Guibas, P. Hanrahan, Q. Huang, Z. Li, S. Savarese, M. Savva, S. Song, H. Su *et al.*, "Shapenet: An information-rich 3D model repository," *arXiv preprint arXiv:1512.03012*, 2015.
- [92] Z. Wu, S. Song, A. Khosla, F. Yu, L. Zhang, X. Tang, and J. Xiao, "3D shapenets: A deep representation for volumetric shapes," in *IEEE CVPR*, 2015, pp. 1912–1920.
- [93] J. J. Lim, H. Pirsiavash, and A. Torralba, "Parsing ikea objects: Fine pose estimation," in *IEEE ICCV*, 2013, pp. 2992–2999.
- [94] Y. Xiang, R. Mottaghi, and S. Savarese, "Beyond pascal: A benchmark for 3d object detection in the wild," in *IEEE WACV*. IEEE, 2014, pp. 75–82.
- [95] T. Zhou, M. Brown, N. Snavely, and D. G. Lowe, "Unsupervised learning of depth and ego-motion from video," in *IEEE CVPR*, vol. 2, no. 6, 2017, p. 7.
- [96] A. Tonioni, M. Poggi, S. Mattoccia, and L. Di Stefano, "Unsupervised adaptation for deep stereo," in *IEEE ICCV*. IEEE, 2017, pp. 1614–1622.
- [97] J. T. Barron, "A more general robust loss function," *arXiv preprint arXiv:1701.03077*, 2017.
- [98] M. Bai, W. Luo, K. Kundu, and R. Urtasun, "Exploiting semantic information and deep matching for optical flow," in *ECCV*. Springer, 2016, pp. 154–170.
- [99] Z. Wang, A. C. Bovik, H. R. Sheikh, and E. P. Simoncelli, "Image quality assessment: from error visibility to structural similarity," *IEEE transactions on image processing*, vol. 13, no. 4, pp. 600–612, 2004.
- [100] S. Vijayanarasimhan, S. Ricco, C. Schmid, R. Sukthankar, and K. Fragkiadaki, "Sfm-net: Learning of structure and motion from video," *arXiv preprint arXiv:1704.07804*, 2017.
- [101] M. Perriollat, R. Hartley, and A. Bartoli, "Monocular template-based reconstruction of inextensible surfaces," *IJCV*, vol. 95, no. 2, pp. 124–137, 2011.
- [102] P. P. Srinivasan, R. Garg, N. Wadhwa, R. Ng, and J. T. Barron, "Aperture supervision for monocular depth estimation," in *IEEE CVPR*, June 2018.
- [103] J. T. Todd and J. F. Norman, "The visual perception of 3-d shape from multiple cues: Are observers capable of perceiving metric structure?" *Perception & Psychophysics*, vol. 65, no. 1, pp. 31–47, 2003.
- [104] K. Xian, C. Shen, Z. Cao, H. Lu, Y. Xiao, R. Li, and Z. Luo, "Monocular relative depth perception with web stereo data supervision," in *IEEE CVPR*, June 2018.
- [105] Y. Kuznetsov, J. Stuckler, and B. Leibe, "Semi-supervised deep learning for monocular depth map prediction," in *IEEE CVPR*, 2017, pp. 6647–6655.

- [106] A. Atapour-Abarghouei and T. P. Breckon, "Real-time monocular depth estimation using synthetic data with domain adaptation via image style transfer," in *IEEE CVPR*, June 2018.
- [107] C. Zheng, T.-J. Cham, and J. Cai, "T2net: Synthetic-to-realistic translation for solving single-image depth estimation tasks," in *ECCV*, September 2018.
- [108] X. Guo, H. Li, S. Yi, J. Ren, and X. Wang, "Learning monocular depth by distilling cross-domain stereo networks," in *ECCV*, September 2018.
- [109] G. Hinton, O. Vinyals, and J. Dean, "Distilling the knowledge in a neural network," *arXiv preprint arXiv:1503.02531*, 2015.
- [110] J. Nath Kundu, P. Krishna Uppala, A. Pahuja, and R. Venkatesh Babu, "Adadepth: Unsupervised content congruent adaptation for depth estimation," in *IEEE CVPR*, June 2018.
- [111] A. Kuzmin, D. Mikushin, and V. Lempitsky, "End-to-end learning of cost-volume aggregation for real-time dense stereo," in *International Workshop on Machine Learning for Signal Processing (MLSP)*. IEEE, 2017, pp. 1–6.
- [112] R. Zabih and J. Woodfill, "Non-parametric local transforms for computing visual correspondence," in *ECCV*. Springer, 1994, pp. 151–158.
- [113] H. Zhan, R. Garg, C. Saroj Weerasekera, K. Li, H. Agarwal, and I. Reid, "Unsupervised learning of monocular depth estimation and visual odometry with deep feature reconstruction," in *IEEE CVPR*, June 2018.
- [114] D. Xu, E. Ricci, W. Ouyang, X. Wang, and N. Sebe, "Multi-scale continuous CRFs as sequential deep networks for monocular depth estimation," in *IEEE CVPR*, 2017, pp. 5354–5362.
- [115] J. Xie, R. Girshick, and A. Farhadi, "Deep3d: Fully automatic 2D-to-3D video conversion with deep convolutional neural networks," in *ECCV*. Springer, 2016, pp. 842–857.
- [116] R. Wang, J.-M. Frahm, and S. M. Pizer, "Recurrent neural network for learning densedepth and ego-motion from video," *arXiv preprint arXiv:1805.06558*, 2018.